Journal of Computational and Applied Mathematics 399 (2022) 113715

Contents lists available at ScienceDirect

Journal of Computational and Applied Mathematics

journal homepage: www.elsevier.com/locate/cam

Finite element simulation of quasi-static tensile fracture in nonlinear strain-limiting solids with the phase-field approach

Sanghyun Lee [a], Hyun Chul Yoon [b,c,*], S.M. Mallikarjunaiah [b]

[a] *Department of Mathematics, Florida State University, 208 Love Building 1017 Academic Way Tallahassee, FL 32306, United States of America*

[b] *Department of Mathematics & Statistics, Texas A&M University-Corpus Christi, 6300 Ocean Drive, Unit 5825, Corpus Christi, TX 78412-5825, United States of America*

[c] *Petroleum & Marine Division, Korea Institute of Geoscience and Mineral Resources, 124 Gwahak-ro, Daejeon 34132, Republic of Korea*

A R T I C L E I N F O

Article history:
Received 11 May 2020
Received in revised form 23 March 2021

Keywords:
Strain-limiting model
Nonlinear elasticity
LEFM
Fracture propagation
Phase-field
Finite element method

A B S T R A C T

We investigate a quasi-static tensile fracture in nonlinear strain-limiting solids by coupling with the phase-field approach. A classical model for the growth of fractures in an elastic material is formulated in the framework of linear elasticity for deformation systems. This linear elastic fracture mechanics (LEFM) model is derived based on the assumption of small strain. However, the boundary value problem formulated within the LEFM and under traction-free boundary conditions predicts large singular crack-tip strains. Fundamentally, this result is directly in contradiction with the underlying assumption of small strain. In this work, we study a theoretical framework of nonlinear strain-limiting models, which are algebraic nonlinear relations between stress and strain. These models are consistent with the basic assumption of small strain. The advantage of such framework over the LEFM is that the strain remains bounded even if the crack-tip stress tends to the infinity. Then, employing the phase-field approach, the distinct predictions for tensile crack growth can be governed by the model. Several numerical examples to evaluate the efficacy and the performance of the model and numerical algorithms structured on finite element method are presented. Detailed comparisons of the strain, fracture energy with corresponding discrete propagation speed between the nonlinear strain-limiting model and the LEFM for the quasi-static tensile fracture are discussed.

1. Introduction

Fracture mechanics has been one of major research interests in several different areas such as civil, mechanical, environmental, petroleum engineering fields and applied mathematics. Initially, Griffith [1] gave a solid foundation for the linear elastic fracture mechanics (LEFM). This energy-based brittle fracture theory was modeled on energy balance between the stored elastic energy of a material and the energy required to create a new crack increment. It has been one of the widely utilized and successful theories in applied mechanics, and many mathematical problems of material failure or fracture were conventionally modeled within the framework of LEFM.

---

[*] Corresponding author at: Petroleum & Marine Division, Korea Institute of Geoscience and Mineral Resources, 124 Gwahak-ro, Daejeon 34132, Republic of Korea.

E-mail addresses: lee@math.fsu.edu (S. Lee), hyun.yoon@kigam.re.kr (H.C. Yoon), M.Muddamallappa@tamucc.edu (S.M. Mallikarjunaiah).

https://doi.org/10.1016/j.cam.2021.113715

However, the LEFM model, when coupled with an idealized zero-traction crack–surface boundary condition, contains a noticeable inconsistency. It predicts the crack-tip strain singularity even though the model is predicated upon infinitesimal strains [2]. The assumption of uniform infinitesimal strains leads to the constitutive relation of the LEFM and thereby it reduces to a linear relationship between the Cauchy stress and strain tensors. The study of fracture within the theory of finite elasticity also resulted in singular stress and strain at the crack-tip [3]. It has been argued for a long time that the erroneous prediction of crack-tip strain singularity may be a consequence of modeling error in the LEFM.

Many studies have attempted to correct the inconsistency by augmenting the LEFM based on different modeling paradigms, such as the cohesive/process zone models [2,4], or surface mechanics-based theories [5–13]. However, some of these methods are based on introducing a separate conceptual zone or utilizing different models. On the other hand, the insufficiency of the LEFM can be further illuminated regarding many new engineering materials as well. There are some clear experimental evidences that certain materials such as the titanium alloy manifest the nonlinear behaviors well within the small strain regime [14–17]. However, the classical linear model cannot properly describe the nonlinear response from stress even when strains are only around 2% [18,19]. Hence, it is also important to provide and study some new class of elasticity models that can capture the stress–strain relationship of such nonlinear materials.

Recently, a new class of nonlinear theoretical models – derived from the implicit relationship between the Cauchy stress and the Cauchy–Green stretch tensors – has been introduced in [20–22]. Structured on the implicit relationship and by appealing to the standard linearization process under the assumption that the norm of the displacement gradient is small, one can arrive at a non-customary nonlinear relationship between the linearized strain and the Cauchy stress tensors. Structured on this nonlinear relation, the strain can remain bounded even if the stress tends theoretically to the infinity. Such a class of nonlinear models is known as the nonlinear strain-limiting models [23–25]. Rigorous mathematical analyses to show the existence of weak solutions for variety of problems formulated within the implicit theory of elasticity are shown in [26–28]. Convergence analysis of the numerical schemes for crack problems are described in [29,30]. Moreover, by employing the nonlinear elasticity within the general strain-limiting theory, the responses of elastic bodies [31–33], electro-elastic bodies [34], magneto-elastic bodies [35], and thermo-elastic bodies [36] are presented in previous studies.

In this study, our main focus is on coupling the strain-limiting model with the phase-field approach to investigate a quasi-static tensile fracture propagation. Recently, the phase-field or the regularized crack method has become a powerful tool to simulate the evolution of cracks and fractures in elastic materials. In particular, the phase-field formulation derived from the variational theory has received a lot of attention from the applied mechanics community due to its strong ties to the Griffith's theory for brittle fracture [37,38]. The advantages of this approach include the ability for automatically determining direction – joining and branching – of crack propagation through minimization of an energy functional without any additional constitutive rules or criteria. Thus, computing the stress intensity factor near the crack-tip is intrinsically embedded in the model. In addition, all computations are performed entirely on the initial, un-deformed configuration and there is no need to disconnect, remove, move elements or introduce additional discontinuity. This feature results in a significant simplification of numerical implementation to handle realistic heterogeneous properties of solid or porous media with adaptive mesh refinements in two and three dimensional applications. Furthermore, recent advances and numerical studies for treating the multiphysical phase-field fractures include the following: thermal shocks and thermo-elastic–plastic solids [39–41], elastic gelatin for wing crack formation [42], pressurized fractures [43,44], fluid-filled (i.e., hydraulic) fractures [45–50], proppant-filled fractures [51], variably saturated porous media [52], crack initiations with microseismic probability maps [53,54], and many other applications [55–62].

To couple the nonlinear strain-limiting model with the phase-field approach for the quasi-static tensile (or mode I) fracture propagation, we employ an iterative coupling algorithm, the staggered L-scheme [63]. The algorithm provides an efficient iterative coupling between the phase-field and the nonlinear mechanics. An adaptive mesh refinement to localize the mesh refining the regularized fractures is applied for the efficiency of the algorithm as in [64]. Then, several numerical simulations are illustrated to compare between the LEFM and the nonlinear strain-limiting elasticity — the convergence of the iterative solvers, stress–strain values, and the fracture propagation along with their energies and discrete crack speed. In summary, the main novelty of this study is to extend the strain-limiting theory to consider the quasi-static fracture initiation and its propagation. Thus, a new computational framework of formulating a quasi-static strain-limiting fracture by iteratively coupling the nonlinear strain-limiting model with the phase-field approach is established.

The organization of the paper is as follows: In Section 2, we briefly introduce the derivation of strain-limiting model and recapitulate the main idea of phase-field approach. Moreover, the mathematical models and governing system for our problem are discussed. Spatial and temporal discretizations using finite element method and the solution algorithm are presented in Section 3. Finally, several numerical examples comparing the classical linear elasticity (i.e., the LEFM) and the nonlinear strain-limiting models for the quasi-static fracture propagation are illustrated in Section 4.

2. Mathematical model

In this section, a brief overview of the physical modeling including the nonlinear strain-limiting elasticity and the phase-field approach is presented structured on previous studies. We first introduce the kinematical setting and notations that we use for the LEFM and the nonlinear strain-limiting models.

2.1. Strain-limiting theories for elasticity

The strain-limiting model for elasticity which was established and discussed in [20–22,24,65] is briefly described in this section. Let $\mathbf{x} := f(\mathbf{X}, t)$ denote the current position of a particle (motion of a particle) that is at $\mathbf{X}$ of a material body $\mathcal{A}$ in the stress-free reference configuration. Here, f is a deformation of the body which is differentiable and the displacement is denoted by $\mathbf{u} := \mathbf{x} - \mathbf{X}$. Then, the displacement gradients are defined

$$\frac{\partial \mathbf{u}}{\partial \mathbf{X}} := \nabla_{\mathbf{X}} \mathbf{u} = \mathbf{F} - \mathbf{I} \quad \text{and} \quad \frac{\partial \mathbf{u}}{\partial \mathbf{x}} := \nabla_{\mathbf{x}} \mathbf{u} = \mathbf{I} - \mathbf{F}^{-1}, \tag{1}$$

where $\mathbf{I}$ is the identity tensor and $\mathbf{F}$ is the deformation gradient

$$\mathbf{F} := \frac{\partial f}{\partial \mathbf{X}}. \tag{2}$$

The left and right Cauchy–Green stretch tensors $\mathbf{B}$ and $\mathbf{C}$ are given by

$$\text{(left)} \;\; \mathbf{B} := \mathbf{F}\mathbf{F}^{\mathrm{T}}, \quad \text{(right)} \;\; \mathbf{C} := \mathbf{F}^{\mathrm{T}}\mathbf{F}, \tag{3}$$

respectively. Then, the Green–St.Venant strain tensor $\mathbf{E}$ and the Almansi–Hamel strain $\mathbf{e}$ are defined as

$$\mathbf{E} := \frac{1}{2}(\mathbf{C} - \mathbf{I}) \quad \text{and} \quad \mathbf{e} := \frac{1}{2}(\mathbf{I} - \mathbf{B}^{-1}). \tag{4}$$

2.1.1. The linearized theory of elasticity for isotropic bodies

Let $\boldsymbol{\sigma}$ denote the Cauchy stress tensor in a deformed configuration, then the first and second Piola–Kirchhoff stress tensors in a reference configuration are

$$\mathbf{S} := \det(\mathbf{F})\mathbf{F}^{-1}\boldsymbol{\sigma} \;\; \text{and} \;\; \bar{\mathbf{S}} := \mathbf{S}\mathbf{F}^{-T}, \tag{5}$$

respectively. The material body $\mathcal{A}$ is called Cauchy elastic if its constitutive class is determined by a scalar function of the deformation gradient, i.e.,

$$\mathbf{S} = \tilde{\mathbf{S}}(\mathbf{F}). \tag{6}$$

Thus, the Cauchy stress $\boldsymbol{\sigma}$ is a function of the deformation gradient $\mathbf{F}$, and the stress depends on the stress-free and final configurations of the body [66]. For a compressible homogeneous isotropic Cauchy elastic body, the constitutive relation [66] is

$$\boldsymbol{\sigma} = \alpha_1 \mathbf{I} + \alpha_2 \mathbf{B} + \alpha_3 \mathbf{B}^2, \tag{7}$$

where α_i, $i = 1, 2, 3$ depend on isotropic invariants of ρ, $\mathrm{tr}(\mathbf{B})$, $\mathrm{tr}(\mathbf{B}^2)$, and $\mathrm{tr}(\mathbf{B}^3)$, where ρ is the density of the body, and $\mathrm{tr}(\cdot)$ is the trace operator.

Next, the body $\mathcal{A}$ is called Green elastic (or hyper-elastic) [67] if the stress response function is the gradient of a scalar valued potential, i.e.,

$$\hat{\mathbf{S}}(\mathbf{F}) = \partial_{\mathbf{F}} \hat{w}(\mathbf{F}), \tag{8}$$

and hence a stored energy, $\hat{w}(\mathbf{F})$, exists. Thus, the stress in a Cauchy elastic body and the stored energy associated with a Green elastic body depend only on the deformation gradient as discussed in [68].

2.1.2. Implicit and strain-limiting constitutive models

A general class of elastic materials than Cauchy or Green elastic bodies, which assumes that the stress and the deformation gradient are related by implicit constitutive relations, is introduced by Rajagopal in [20,21]. A special subclass of these implicit models is an explicit representation where the left Cauchy–Green stretch tensor $\mathbf{B}$ is given in terms of Cauchy stress $\boldsymbol{\sigma}$. These models for elastic bodies are neither Cauchy elastic nor Green elastic.

First, let us consider an isotropic implicit constitutive relation of the form

$$\mathcal{F}(\boldsymbol{\sigma}, \mathbf{B}) = \mathbf{0}, \tag{9}$$

between the Cauchy stress and the left Cauchy–Green tensor. Following [69], with the assumption that the elastic body is isotropic homogeneous compressible, we obtain

$$\mathbf{B} = \tilde{\alpha}_1 \mathbf{I} + \tilde{\alpha}_2 \boldsymbol{\sigma} + \tilde{\alpha}_3 \boldsymbol{\sigma}^2, \tag{10}$$

where $\tilde{\alpha}_i$, $i = 1, 2, 3$ are the scalar-valued functions of the isotropic invariants of ρ, $\mathrm{tr}(\boldsymbol{\sigma})$, $\mathrm{tr}(\boldsymbol{\sigma}^2)$, and $\mathrm{tr}(\boldsymbol{\sigma}^3)$. Note that the stress and the left Cauchy–Green stretch are reversed compared to the classical model in Eq. (7). Eq. (10) cannot be obtained from the class of general Cauchy elastic bodies by inverting the stress as a function of the deformation gradient [21]. Under the assumption of small displacement gradient such that

$$\max \|\nabla_{\mathbf{x}} \mathbf{u}\| = \mathbf{0}(\delta), \;\; \delta \ll 1, \tag{11}$$

we obtain

$$\mathbf{E} = \boldsymbol{\epsilon} + \mathbf{0}(\delta^2), \quad \mathbf{e} = \boldsymbol{\epsilon} + \mathbf{0}(\delta^2), \quad \mathbf{B} = \mathbf{I} + 2\boldsymbol{\epsilon} + \mathbf{0}(\delta^2), \tag{12}$$

where $\boldsymbol{\epsilon}$ is the linearized strain:

$$\boldsymbol{\epsilon} := \boldsymbol{\epsilon}(\mathbf{u}) = \frac{1}{2}\left(\nabla\mathbf{u} + (\nabla\mathbf{u})^{\mathrm{T}}\right), \tag{13}$$

where $(\cdot)^{\mathrm{T}}$ is the transpose of $(\cdot)$. Finally, the linearization of the model, Eq. (10), under the assumption of small displacement gradient (Eqs. (11)–(12)) leads to

$$\boldsymbol{\epsilon} = \beta_1\mathbf{I} + \beta_2\boldsymbol{\sigma} + \beta_3\boldsymbol{\sigma}^2, \tag{14}$$

where the linearized strain is given as a nonlinear function of the Cauchy stress and here the β_1 is dimensionless coefficient and material moduli β_2 and β_3 need to have dimensions that are the inverse of the stress and the square of the stress, respectively.

The above approximation, Eq. (14), has no restrictions on the stress while requiring the strain still to be small. This nonlinear relationship can be crucial since bounded strain can be obtained even if the stress tends to a large value. Such models have very interesting applications, particularly dealing with crack and notch problems – which may lead to unrealistic singular strains within the classical linearized elasticity.

Remark 2.1. Under the assumption of Eq. (11), we note that there is no distinction between $\mathbf{E}$, $\mathbf{e}$ and $\boldsymbol{\epsilon}$, and we do not distinguish between the reference (or the undeformed) and the deformed configurations for linear elastic materials.

Remark 2.2. For the isotropic linear elastic material in the absence of body forces, the linear and angular momentum balance reduces to

$$-\nabla\cdot\boldsymbol{\sigma} = \mathbf{0}, \quad \boldsymbol{\sigma} = \boldsymbol{\sigma}^T. \tag{15}$$

If the displacement (including in the neighborhood of stress concentrators as crack-tips, reentrant notch-tips, etc.) is smooth enough, one can consider formulating boundary value problem using (15). Further, the linearized strain tensor needs to satisfy the compatibility conditions such as

$$\operatorname{curl}(\operatorname{curl}\boldsymbol{\epsilon}) = \mathbf{0}, \tag{16}$$

where curl is the classical operator for tensors and $(\operatorname{curl}\mathbf{A})_{ij} = \mathbf{e}_{ilk}\dfrac{\partial A_{lj}}{\partial x_k}$, where $\mathbf{e}$ is the standard basis vector in a given Euclidean space. Eq. (16) implies that the displacement in a simply-connected body without any overlaps or gaps can be obtained by the integration of the linearized strain. In the view of Eq. (15), Eq. (16) will be automatically satisfied for a linear elastic material.

For an isotropic, homogeneous, linear elastic material, the constitutive relationship for the Cauchy stress is given by the Hooke's law

$$\boldsymbol{\sigma} = 2\mu\,\boldsymbol{\epsilon} + \lambda\operatorname{tr}(\boldsymbol{\epsilon})\,\mathbf{I}, \tag{17}$$

where μ and λ are Lamé parameters and $\operatorname{tr}(\cdot)$ is the trace operator for tensors. Since Eq. (17) is invertible, we can express linearized strain tensor $\boldsymbol{\epsilon}$ as a (linear) function of the Cauchy stress

$$\boldsymbol{\epsilon} = \frac{1}{2\mu}\boldsymbol{\sigma} - \frac{\lambda}{6\mu(\lambda + (2/3)\mu)}\operatorname{tr}(\boldsymbol{\sigma})\,\mathbf{I}. \tag{18}$$

Hence, one can formulate the boundary value problems for the linear elastic material either within Eq. (17) or Eq. (18). However, it may lead to the fact that the strains in the neighborhood of crack-tips will be large, which clearly violates the fundamental assumption of Eq. (11), which is a consequence of the derived theory of linear elastic materials. In Eq. (18) for elastic materials, the shear modulus μ is always positive and the term $\lambda + (2/3)\mu$, called the bulk modulus (which has the same unit as stress), cannot be zero.

Now, let us consider the special subclass of strain-limiting constitutive relationship from Eq. (14), having the form

$$\boldsymbol{\epsilon} = \Psi_0\left(\operatorname{tr}(\boldsymbol{\sigma}), |\boldsymbol{\sigma}|\right)\mathbf{I} + \Psi_1\left(|\boldsymbol{\sigma}|\right)\boldsymbol{\sigma}, \tag{19}$$

and which is generally non-invertible. In the above Eq. (19), $\Psi_0(\cdot,\cdot)$, $\Psi_1(\cdot)$ are scalar functions of stress invariants, and more importantly, the assumption of no residual stress implies $\Psi_0(0,\cdot) = 0$.

In this paper, we extend these previous frameworks for static cracks [70–72] to a quasi-static crack evolution by considering a special subclass of nonlinear models that are invertible, yet rank-one convex [73,74], and strongly elliptic when the strains are small [73]. To that end, let us consider a nonlinear, hyperelastic model in the infinitesimal strain regime:

$$\mathbf{E} = \phi(\mathbb{K}[\bar{\mathbf{S}}])\mathbb{K}[\bar{\mathbf{S}}], \tag{20}$$

where $\mathbb{K}$ is the fourth-order compliance tensor, $\mathbf{E}$ is the Green–Lagrangian strain, and $\bar{\mathbf{S}}$ is the second Piola–Kirchhoff stress. Note that the above model can be customized for an anisotropic material model and it was shown in [75] that the models of the type, Eq. (20), fail to be rank-one convex (or, equivalently, lose the notion of strong ellipticity) if the strains are large. A simpler model to consider within the general class of models described by Eq. (20) is

$$\phi(\mathbb{K}[\bar{\mathbf{S}}]) := \tilde{\phi}(|\mathbb{K}^{1/2}[\bar{\mathbf{S}}]|), \tag{21}$$

as described in [72]. In Eq. (21), $\tilde{\phi}(r)$ is a positive, monotonic decreasing function and $r\tilde{\phi}(r)$ is uniformly bounded for $0 < r < \infty$, and $\mathbb{K}^{1/2}[\cdot]$ denotes the unique, positive definite square-root of the compliance tensor $\mathbb{K}$. One special case of Eq. (21) is defined with

$$\tilde{\phi}(r) := \frac{1}{(1+(\beta r)^{\alpha})^{1/\alpha}}, \tag{22}$$

where α and β are the nonlinear model parameters [26,70–72]. Some detailed studies of these parameters are presented in the numerical example section.

Remark 2.3. The function $\tilde{\phi}(r)$ in (22) needs to be a decreasing function with $\beta > 0$ and $\alpha > 0$ for the strains to be "limited" near the crack-tip. Using the function $\tilde{\phi}(r)$, one can fix an upper bound for strains a priori to model specific materials or physical experiments with real data. The assumption of β being positive is very important for the model to be hyperelastic and invertible, and the same has been observed in several other studies involving strain-limiting models [26–29,76,77].

Thus, under the infinitesimal strain assumption, we arrive at the *nonlinear relation* between strain $\boldsymbol{\epsilon}$ and stress, such as

$$\boldsymbol{\epsilon} = \tilde{\phi}(|\mathbb{K}^{1/2}[\bar{\mathbf{S}}]|)\mathbb{K}[\bar{\mathbf{S}}], \tag{23}$$

where $\bar{\mathbf{S}}$ can be viewed as the Cauchy stress, i.e., $\mathbb{K}[\bar{\mathbf{S}}] = \mathbb{K}[\boldsymbol{\sigma}]$. Then, we have

$$\boldsymbol{\epsilon} = \tilde{\phi}(|\mathbb{K}^{1/2}[\boldsymbol{\sigma}]|)\mathbb{K}[\boldsymbol{\sigma}], \tag{24}$$

and from the relation in Eq. (18), we obtain

$$\mathbb{K}[\boldsymbol{\sigma}] := \frac{\boldsymbol{\sigma}}{2\mu} - \frac{\lambda\,\mathrm{tr}(\boldsymbol{\sigma})\,\mathbf{I}}{2\mu(2\mu+3\lambda)}, \tag{25}$$

where $\boldsymbol{\sigma}$ is obtained from Eq. (17). Finally, by using Eqs. (22)–(25), we obtain the following nonlinear relation for the strain $\boldsymbol{\epsilon}$ by

$$\boldsymbol{\epsilon} := \boldsymbol{\epsilon}_{\mathrm{NL}} = \frac{\mathbb{K}[\boldsymbol{\sigma}]}{(1+(\beta|\mathbb{K}^{1/2}[\boldsymbol{\sigma}]|)^{\alpha})^{1/\alpha}}, \tag{26}$$

where

$$|\mathbb{K}^{1/2}[\boldsymbol{\sigma}]| = \left(\frac{\boldsymbol{\sigma}:\boldsymbol{\sigma}}{2\mu} - \frac{\lambda\,\mathrm{tr}(\boldsymbol{\sigma})^2}{2\mu(2\mu+3\lambda)}\right)^{1/2}.$$

We note that the strain $\boldsymbol{\epsilon}$ is denoted in two different forms depending on the formulations. The nonlinear strain-limiting strain (denoted as $\boldsymbol{\epsilon}_{\mathrm{NL}}$) is the same as $\boldsymbol{\epsilon}$ in Eq. (18) provided $\beta = 0$ or $\alpha \to \infty$. Henceforth, unless otherwise noted, we use the notation $\boldsymbol{\epsilon}_{\mathrm{NL}}$ only for the strain obtained by the nonlinear model.

To formulate boundary value problems within the framework of the new class of nonlinear models, we start by setting the displacement ($\mathbf{u}$) as the primary variable as expressed in Eq. (13). Here, the strain compatibility condition (Eq. (16)) is automatically satisfied. Then, we invert the relation of Eq. (24) to get the stress tensor components, and replace components in Eq. (15) with these to obtain a quasi-linear partial differential equation. Recently, it was shown in [70–72,78] that models within the context of Eq. (19) for the problem of a static crack in a body under the anti-plane shear lead to solutions with the bounded strains at the crack-tip. In addition, a model for the evolution of quasi-static crack under the same type of loading is developed in [79]. It was shown that the crack-tip strain does not grow in the same order as the linear model and the result is consistent with the linearization assumption used in the derivation of the model.

Then, since Eq. (26) is invertible and letting $\bar{\mathbf{S}} = \boldsymbol{\sigma}$ to formulate in a deformed configuration, the partial differential equation in the form of Eq. (15) for the proposed strain-limiting model is derived as

$$-\nabla\cdot\frac{\mathbb{E}[\boldsymbol{\epsilon}]}{(1-(\beta|\mathbb{E}^{1/2}[\boldsymbol{\epsilon}]|)^{\alpha})^{1/\alpha}} = \mathbf{0}. \tag{27}$$

Here $\mathbb{E}$ is the fourth-order linearized elasticity tensor and is symmetric and positive definite. For the isotropic, homogeneous materials, we have

$$\mathbb{E}[\boldsymbol{\epsilon}] := \boldsymbol{\sigma} = 2\,\mu\,\boldsymbol{\epsilon} + \lambda\,\mathrm{tr}(\boldsymbol{\epsilon})\,\mathbf{I}, \tag{28}$$

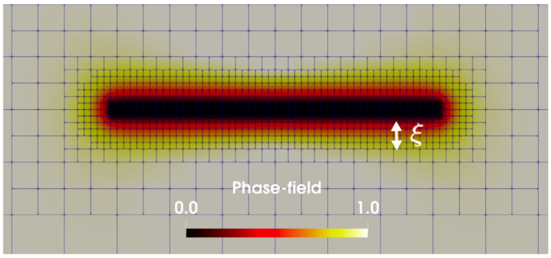

Fig. 1. An example of a fracture defined with the phase-field function $\varphi(\cdot,t) \in [0.1]$.

by considering the displacement as the primary unknown variable, and $\boldsymbol{\epsilon}$ is given as the symmetric gradient of the displacement (Eq. (13)). The other method to directly compute the explicit nonlinear stress by using the Airy stress function is shown in [79–82].

Remark 2.4. From Eq. (27), it is required to satisfy the following condition,

$$\left(1-\left(\beta|\mathbb{E}^{1/2}[\boldsymbol{\epsilon}]|\right)^{\alpha}\right)^{1/\alpha} > 0, \tag{29}$$

for the ellipticity for the weak formulation. This condition is similar to the results provided in [29,76,77] for their analyses. We note that this condition is related to the mechanical properties such as Lamé coefficients within the calculation of $|\mathbb{E}^{1/2}[\boldsymbol{\epsilon}]|$ and the choice of the nonlinear parameters, α and β. More detailed conditions particularly regarding the strain-limiting effects are addressed in Section 4.

2.2. Phase-field approach for fracture propagation with nonlinear strain-limiting elasticity

Let $\Lambda := \Lambda(t) \in \mathbb{R}^d$ ($d = 2, 3$) be a smooth open and bounded computational domain, with a given boundary $\partial\Lambda$. Here, the time is denoted by $t \in [0, T]$, with the final time $T > 0$ in the computational time interval. As discussed in [83,84], the fracture $\mathcal{C}(t)$ is contained compactly in $\Lambda(t)$. In the phase-field fracture approach, discontinuities in the displacement field $\mathbf{u}$ across the lower-dimensional crack surface is approximated by a smooth scalar function $\varphi(\cdot,t) : \Lambda\times[0,T] \to [0,1]$. This phase-field function $\varphi(\cdot,t)$ introduces a diffusive transition zone, which has a bandwidth ξ for regularization, between the fractured region (Ω_F) having $\varphi(\cdot,t) = 0$ and the un-fractured (or intact) region (Ω_R) having $\varphi(\cdot,t) = 1$. See Fig. 1 for more details. The boundary of the fracture is denoted by $\Gamma_F(t) := \bar{\Omega}_F(t) \cap \bar{\Omega}_R(t)$.

To discuss the phase-field fracture, we first introduce the Francfort–Marigo functional [84], which describes the energy with a fracture in an elastic body as

$$E(\mathbf{u},\mathcal{C}) = \frac{1}{2}\int_{\Omega_R} \boldsymbol{\sigma}(\mathbf{u}) : \boldsymbol{\epsilon}(\mathbf{u})\, d\mathbf{x} + G_c H^{d-1}(\mathcal{C}), \tag{30}$$

where $\mathbf{u}(\cdot,t) : \Omega_R \times [0,T] \to \mathbb{R}^d$ is the solid's displacement, $\boldsymbol{\sigma}(\mathbf{u})$ is the Cauchy stress tensor and $\boldsymbol{\epsilon}(\mathbf{u})$ is the linearized strain tensor. Here the first term in the right-hand side is the strain energy in an un-fractured region and the second term is the fracture energy, where the Hausdorff measure $H^{d-1}(\mathcal{C})$ denotes one dimension less fracture scale such as the length of the fracture in two-dimensional domain and is multiplied by G_c, i.e., the critical energy release rate.

Next, we consider the global constitutive dissipation functional of Ambrosio–Tortorelli type [85,86] to regularize the total energy with the introduction of a phase-field function. Eq. (30) is rewritten as the global dissipation formulation such as

$$E_\xi(\mathbf{u},\varphi) = \frac{1}{2}\int_\Lambda ((1-\kappa)\varphi^2+\kappa)\,\boldsymbol{\sigma}(\mathbf{u}) : \boldsymbol{\epsilon}(\mathbf{u})\, d\mathbf{x} + G_c\int_\Lambda \left(\frac{1}{2\xi}(1-\varphi)^2 + \frac{\xi}{2}|\nabla\varphi|^2\right) d\mathbf{x}, \tag{31}$$

where all definitions are extended to Λ. Finally, we seek the solution $\mathbf{u}$ and φ which minimizes the energy functional $E_\xi(\mathbf{u},\varphi)$, i.e., find $\{\mathbf{u},\varphi\}$ such that

$$\min_{\mathbf{u},\varphi} E_\xi(\mathbf{u},\varphi), \tag{32}$$

of which approach was initially introduced for linear elasticity in [83,84,87]. In addition, the convergence of time discrete solutions of Eq. (32) to continuous solutions as timestep goes to zero was discussed in [88,89]. This approach becomes as a variational inequality since the fracture propagation is required to satisfy a crack irreversibility constraint, which is given as $\partial_t\varphi(\cdot,t) < 0$. This condition only allows the phase-field value to decrease in time and enforces the fracture to only propagate but not to be healed. The phase-field function is subject to homogeneous Neumann conditions on $\partial\Lambda$. For the quasi-static system, the initial domains, $\Omega_F(\cdot,0)$ and $\Omega_R(\cdot,0)$, are defined by a given initial phase-field value $\varphi(\cdot,0)$, either by 0 or 1.

We note that the previous numerical results of phase-field approach in [42,46,50] employ the classical linear elasticity with the LEFM such as

$$\boldsymbol{\sigma}(\mathbf{u}) = 2\mu\boldsymbol{\epsilon}(\mathbf{u}) + \lambda(\nabla\cdot\mathbf{u})\mathbf{I}, \tag{33}$$

and several numerical examples illustrate large stress thus large strain values near the crack-tip. In this study aiming to overcome the issue, we extend the nonlinear strain-limiting theory to the quasi-static fracture model. In the associated strain energy function of Eq. (31), the linear elastic stress tensor Eq. (33) will be replaced by the proposed strain-limiting model (Eq. (27)),

$$\boldsymbol{\sigma}(\mathbf{u}) = \frac{\mathbb{E}[\boldsymbol{\epsilon}]}{(1-(\beta|\mathbb{E}^{1/2}[\boldsymbol{\epsilon}]|)^{\alpha})^{1/\alpha}}, \tag{34}$$

where $\alpha, \beta > 0$, and $\mathbb{E}[\boldsymbol{\epsilon}] := 2\,\mu\,\boldsymbol{\epsilon} + \lambda\,\mathrm{tr}(\boldsymbol{\epsilon})\mathbf{I}.$ In this paper, we implement both Eq. (33) and Eq. (34) as two different models – the LEFM and the nonlinear strain-limiting models, respectively – and compare the results.

3. Numerical method

In this section, we present the finite element method utilized for the spatial discretization with the temporal discretization to consider the quasi-static problem and the irreversibility condition. In addition, the Euler–Lagrange formulation for our governing system and the linearization of the given nonlinear problems are discussed. Finally, the coupling between the nonlinear elasticity and the phase-field equations, so-called the L-scheme [63] is presented.

3.1. Temporal discretization and augmented Lagrangian penalization

We define a partition of the time interval $0 =: t^0 < t^1 < \cdots < t^N := T$ and denote the uniform timestep size by $\Delta t := t^n - t^{n-1}$. Then, we denote the temporal discretized solutions by

$$\mathbf{u}^n := \mathbf{u}(\cdot, t^n) \quad \text{and} \quad \varphi^n := \varphi(\cdot, t^n). \tag{35}$$

Here, the irreversibility condition $\partial_t\varphi < 0$ is discretized by $\varphi^n \leq \varphi^{n-1}$ ($\varphi^n - \varphi^{n-1} \leq 0$) with employing the backward Euler method. Due to this irreversibility condition, the energy minimization problem (32) becomes the constrained energy minimization problem. Thus, now we seek for the solution $\mathbf{u}^n$ and φ^n minimizing

$$\min_{\mathbf{u}^n,\varphi^n} E_{\xi}(\mathbf{u}^n, \varphi^n) + \frac{1}{2\gamma}\|[\omega_\gamma + \gamma(\varphi^n - \varphi^{n-1})]^+\|^2, \tag{36}$$

for each timestep n with given φ^{n-1}. The last term is the penalization term to enforce the irreversibility condition as discussed in [63,90]. Here $\gamma > 0$ is the penalization parameter and the choice of γ is very sensitive to the numerical results. If γ is too small, the irreversibility condition will not be enforced enough and if γ is too large, the linear system becomes ill-conditioned. For the better performance, we utilize the augmented Lagrangian method [90–92] by adding a function $\omega_\gamma \in L^2(\Lambda)$ which is given as an initial guess and updated through the iteration. Moreover, here $[\cdot]^+$ denotes the positive part of a function, i.e., $[f]^+ := \max(0, f)$.

3.2. Spatial discretizations and Euler–Lagrange equations

We consider the continuous Galerkin finite element methods for the coupled system. A mesh family $\{\mathcal{T}_h\}_{h>0}$ is assumed to be shape regular in the sense of Ciarlet, and we assume that each mesh $\mathcal{T}_h$ is a subdivision of $\bar{\Lambda}$ made of disjoint elements $\mathcal{K}$, i.e., quadrilaterals when $d = 2$ or hexahedrons when $d = 3$. Each subdivision is assumed to exactly approximate the computational domain, thus $\bar{\Lambda} = \cup_{\mathcal{K}\in\mathcal{T}_h}\mathcal{K}$. The diameter of an element $\mathcal{K} \in \mathcal{T}_h$ is denoted by h and we denote $h_{\min}$ for the minimum. For any integer $k \geq 1$ and any $\mathcal{K} \in \mathcal{T}_h$, we denote by $\mathbb{Q}^k(\mathcal{K})$ the space of scalar-valued multivariate polynomials over $\mathcal{K}$ of partial degree of at most k. The vector-valued counterpart of $\mathbb{Q}^k(\mathcal{K})$ is denoted $\mathbf{Q}^k(\mathcal{K})$. Here, we set $k = 1$ to consider the piecewise bilinear finite elements.

Let $V_h \times W_h$ be the discrete space formulated by the continuous Galerkin approximations where

$$V_h(\mathcal{T}_h) := \{W \in C^0(\bar{\Lambda}; \mathbb{R}^d) \mid W = \mathbf{0} \text{ on } \partial\Lambda, W|_{\mathcal{K}} \in \mathbf{Q}^1(\mathcal{K}), \forall\mathcal{K} \in \mathcal{T}_h\}, \tag{37}$$

$$W_h(\mathcal{T}_h) := \{Z \in C^0(\bar{\Lambda}; \mathbb{R}) |\, Z^n \leq Z^{n-1} \leq 1, Z|_{\mathcal{K}} \in \mathbb{Q}^1(\mathcal{K}), \forall\mathcal{K} \in \mathcal{T}_h\}. \tag{38}$$

The spatial discretized solution variables are $\mathbf{u}_h \in C^1([0, T]; V_h(\mathcal{T}))$ and $\varphi_h \in C^1([0, T]; W_h(\mathcal{T}))$. For simplicity of our presentation, we omit the h-subscript for the displacement and the phase-field, and we only consider the discrete solutions henceforth.

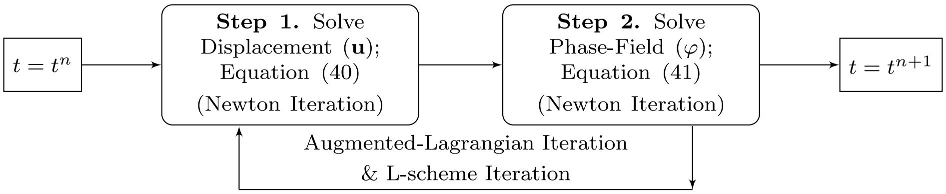

Fig. 2. The global iterative algorithm flowchart.

Next, we formulate the variational form of the energy functional $E_\xi(\mathbf{u}^n, \varphi^n)$ in Eq. (36) by employing the Euler–Lagrange equations and the finite element discretizations. Thus, find $U^n := \{\mathbf{u}^n, \varphi^n\} \in V_h \times W_h$ such that

$$\begin{aligned} A(U^n)(\psi) &= (((1-\kappa)(\varphi^n)^2 + \kappa)\,\boldsymbol{\sigma}(\mathbf{u}^n), \boldsymbol{\epsilon}(\boldsymbol{w})) - G_c(\frac{1}{\xi}(1-\varphi^n), \psi) + G_c(\xi\nabla\varphi^n, \nabla\psi) \\ &\quad + ([\omega_\gamma + \gamma(\varphi^n - \varphi^{n-1})]^+, \psi) = 0, \quad \forall \psi \in \mathit{\Psi} := \{\boldsymbol{w}, \psi\} \in V_h \times W_h, \end{aligned} \tag{39}$$

for each t^n. We note that κ ($0 < \kappa \ll \xi \ll 1$) is a numerical regularization parameter depending on h to ensure the numerical stability [43]. For simplicity, we define the degradation function as

$$g(\varphi) := (1-\kappa)(\varphi^n)^2 + \kappa.$$

Then, by computing the directional derivative of Eq. (39) with respect to $\mathbf{u}$ and φ, we obtain the following subproblems

$$A_1(\mathbf{u}^n, \boldsymbol{w}) := (g(\varphi)\,\boldsymbol{\sigma}(\mathbf{u}^n), \boldsymbol{\epsilon}(\boldsymbol{w})) = 0, \quad \forall \boldsymbol{w} \in V_h, \tag{40}$$

and

$$\begin{aligned} A_2(\varphi^n, \psi) &:= (1-\kappa)(\varphi^n \boldsymbol{\sigma}(\mathbf{u}^n) : \boldsymbol{\epsilon}(\mathbf{u}), \psi) - G_c(\frac{1}{\xi}(1-\varphi^n), \psi) \\ &\quad + G_c(\xi\nabla\varphi^n, \nabla\psi) + ([\omega_\gamma + \gamma(\varphi^n - \varphi^{n-1})]^+, \psi) = 0, \quad \forall \psi \in W_h. \end{aligned} \tag{41}$$

Here, we denote A_1 as the mechanics subproblem and A_2 as the phase-field subproblem. We note that the time-discretized system, Eqs. (40)–(41), was analyzed in [93,94] by showing the existence of one global minimizer $(\mathbf{u}^n, \varphi^n) \in V_h \times W_h$.

3.3. Newton method and iterative algorithm

In this section, we briefly recapitulate and extend the staggered L-scheme introduced in [63] for iteratively coupling the mechanics subproblem (Eq. (40)) and the phase-field subproblem (Eq. (41)). For each timestep n, the iterative algorithm defines a sequence $\{\mathbf{u}^{n,i}, \varphi^{n,i}\}$, where each $i = 1, 2, \dots, N_i$ indicates each iteration step. The L-scheme iteration for our system is formulated with two steps. First, the mechanics subproblem (Eq. (40)) is solved with the given phase-field and displacement values given from the previous iteration, $\{\mathbf{u}^{n,i-1}, \varphi^{n,i-1}\}$. For the first iteration ($i = 1$), we set $\mathbf{u}^{n,i-1} = \mathbf{u}^{n,0} := \mathbf{u}^{n-1}$ ($\varphi^{n,i-1} = \varphi^{n,0} := \varphi^{n-1}$). Then, the phase-field subproblem of Eq. (41) is solved with the displacement value, $\mathbf{u}^{n,i}$. Each nonlinear subproblem is linearized by utilizing the Newton method. For the faster convergence of our nonlinear problem, we note that the linear problem of the LEFM is employed for the initial guess for the initial iteration.

In summary, Fig. 2 illustrates the overall global solution algorithm for our proposed coupled system. We note that the augmented-Lagrangian iteration to update the penalty parameter γ and ω_γ is combined with the L-scheme iteration.

3.3.1. Step 1. Solve the mechanics subproblem

In this section, we describe the details of the solution algorithm with the L-scheme iteration for the mechanics subproblem to find the displacement ($\mathbf{u}$). For each timestep n and for each iteration i, we seek for $\mathbf{u}^{n,i} \in V_h$ with given $\mathbf{u}^{n,i-1}, \varphi^{n,i-1}$ satisfying

$$A_1(\mathbf{u}^{n,i}, \boldsymbol{w}) = 0, \quad \forall \boldsymbol{w} \in V_h, \tag{42}$$

where

$$A_1(\mathbf{u}^{n,i}, w) := (g(\varphi^{n,i-1})\,\boldsymbol{\sigma}(\mathbf{u}^{n,i}), \boldsymbol{\epsilon}(\boldsymbol{w})) + L_u(\mathbf{u}^{n,i} - \mathbf{u}^{n,i-1}, \boldsymbol{w}). \tag{43}$$

Here, the last term is an additional term from the L-scheme iterative method [63] with a given positive parameter L_u.

To solve Eq. (42), we employ the Newton iteration, and we find $\delta\mathbf{u}^{n,i,a} \in V_h$ by solving

$$A_1'(\mathbf{u}^{n,i,a-1}, \varphi^{n,i-1})(\delta\mathbf{u}^{n,i,a}, \boldsymbol{w}) = -A_1(\mathbf{u}^{n,i,a-1})(\boldsymbol{w}), \quad \forall \boldsymbol{w} \in V_h, \tag{44}$$

for the Newton iteration step, $a = 1, 2, \ldots$, until $\|\delta \mathbf{u}^{n,i,a}\| \leq \varepsilon_a$. Then, the Newton update is given by

$$\mathbf{u}^{n,i,a} = \mathbf{u}^{n,i,a-1} + \omega_u \delta \mathbf{u}^{n,i,a}, \tag{45}$$

where $\omega_u \in [0, 1]$ is a line search parameter. If the Newton iteration converges, we set

$$\mathbf{u}^{n,i} = \mathbf{u}^{n,i,a}.$$

Here, the Jacobian of A_1 is computed as

$$A_1'(\mathbf{u}^{n,i,a-1}, \varphi^{n,i-1})(\delta \mathbf{u}^{n,i,a}, \boldsymbol{w}) := (g(\varphi^{n,i-1})\, \boldsymbol{\sigma}(\delta \mathbf{u}^{n,i,a}), \boldsymbol{\epsilon}(\boldsymbol{w})) + L_u(\delta \mathbf{u}^{n,i,a}, \boldsymbol{w}), \tag{46}$$

and

$$A_1(\mathbf{u}^{n,i,a-1}, \boldsymbol{w}) := (g(\varphi^{n,i-1})\, \boldsymbol{\sigma}(\mathbf{u}^{n,i,a-1}), \boldsymbol{\epsilon}(\boldsymbol{w})) + L_u(\mathbf{u}^{n,i,a-1} - \mathbf{u}^{n,i-1}, \boldsymbol{w}). \tag{47}$$

As aforementioned, here we consider two different cases for the choice of $\boldsymbol{\sigma}$. First, for the classical linear elasticity case, we define

$$\boldsymbol{\sigma}(\mathbf{u}^{n,i,a-1}) := \mu \left(\nabla \mathbf{u}^{n,i,a-1} + (\nabla \mathbf{u}^{n,i,a-1})^{\mathrm{T}}\right) + \lambda(\nabla \cdot \mathbf{u}^{n,i,a-1})\mathbf{I}. \tag{48}$$

Next, we recall the nonlinear constitutive relationship between linearized strain and the Cauchy stress. The inverted form of stress by considering the displacement $\mathbf{u}$ as the primary variable is defined as

$$\boldsymbol{\sigma}(\mathbf{u}^{n,i,a-1}) := \frac{\mu \left(\nabla \mathbf{u}^{n,i,a-1} + \left(\nabla \mathbf{u}^{n,i,a-1}\right)^{\mathrm{T}}\right) + \lambda\,(\nabla \cdot \mathbf{u}^{n,i,a-1})\,\mathbf{I}}{\left(1 - \left(\beta |\mathbb{E}^{1/2}\left[\boldsymbol{\epsilon}^{n,i,a-1}\right]|\right)^{\alpha}\right)^{1/\alpha}}, \tag{49}$$

where

$$\begin{aligned} \left|\mathbb{E}^{1/2}\left[\boldsymbol{\epsilon}^{n,i,a-1}\right]\right|^2 &= \mathbb{E}^{1/2}[\boldsymbol{\epsilon}^{n,i,a-1}] \colon \mathbb{E}^{1/2}\left[\boldsymbol{\epsilon}^{n,i,a-1}\right] \\ &= \boldsymbol{\epsilon}^{n,i,a-1} \colon \mathbb{E}^{1/2}[\mathbb{E}^{1/2}\left[\boldsymbol{\epsilon}^{n,i,a-1}\right]] \\ &= \boldsymbol{\epsilon}^{n,i,a-1} \colon \mathbb{E}\left[\boldsymbol{\epsilon}^{n,i,a-1}\right] \\ &= 2\mu \left(\frac{\nabla \mathbf{u}^{n,i,a-1} + (\nabla \mathbf{u}^{n,i,a-1})^{\mathrm{T}}}{2}\right) \colon \left(\frac{\nabla \mathbf{u}^{n,i,a-1} + (\nabla \mathbf{u}^{n,i,a-1})^{\mathrm{T}}}{2}\right) + \lambda \left(\nabla \cdot \mathbf{u}^{n,i,a-1}\right)^2. \end{aligned} \tag{50}$$

Due to the complexity from the nonlinear formulation, the terms in Eq. (46) and Eq. (47) require some computations. In particular, the first term in Eq. (46) is rewritten as

$$\begin{aligned} (g(\varphi^{n,i-1})\boldsymbol{\sigma}(\delta \mathbf{u}^{n,i,a}), \boldsymbol{\epsilon}(\boldsymbol{w})) = &\Bigg(g(\varphi^{n,i-1}) \Bigg(\frac{2\mu \left(\frac{\nabla \delta \mathbf{u}^{n,i,a} + (\nabla \delta \mathbf{u}^{n,i,a})^{\mathrm{T}}}{2}\right) + \lambda\,(\nabla \cdot \delta \mathbf{u}^{n,i,a})\,\mathbf{I}}{\left(1 - \left(\beta |\mathbb{E}^{1/2}\left[\boldsymbol{\epsilon}\right]|\right)^{\alpha}\right)^{1/\alpha}} \\ &+ \frac{\beta^{\alpha} \theta_1\{\mathbf{u}^{n,i,a-1}\} \theta_2\{\mathbf{u}^{n,i,a-1}, \delta \mathbf{u}^{n,i,a}\} \mathbb{E}[\boldsymbol{\epsilon}]}{\left(1 - \beta^{\alpha} |\mathbb{E}^{1/2}\left[\boldsymbol{\epsilon}\right]|^{\alpha}\right)^{1+1/\alpha}} \Bigg) \colon \left(\frac{\nabla \boldsymbol{w} + \nabla \boldsymbol{w}^{\mathrm{T}}}{2}\right) \Bigg), \end{aligned} \tag{51}$$

where

$$\theta_1\{\mathbf{u}\} := \left|\mathbb{E}^{1/2}\left[\boldsymbol{\epsilon}\right]\right|^{\alpha - 2}, \tag{52}$$

$$\begin{aligned} \theta_2\{\mathbf{u}, \delta \mathbf{u}\} &:= \left(\left|\mathbb{E}^{1/2}\left[\boldsymbol{\epsilon}\right]\right|\right)' \\ &= 2\mu \left(\frac{\nabla \mathbf{u} + \nabla \mathbf{u}^{\mathrm{T}}}{2}\right) \colon \left(\frac{\nabla \delta \mathbf{u} + \nabla \delta \mathbf{u}^{\mathrm{T}}}{2}\right) + \lambda\, \left(\nabla \cdot \mathbf{u}\right) \left(\nabla \cdot \delta \mathbf{u}\right). \end{aligned} \tag{53}$$

Moreover, the first term in Eq. (47) is derived as

$$\begin{aligned} &(g(\varphi^{n,i-1})\boldsymbol{\sigma}(\mathbf{u}^{n,i,a-1}), \boldsymbol{\epsilon}(\boldsymbol{w})) \\ &= \left(g(\varphi^{n,i-1}) \left(\frac{2\mu \left(\frac{\nabla \mathbf{u}^{n,i,a-1} + (\nabla \mathbf{u}^{n,i,a-1})^{\mathrm{T}}}{2}\right) + \lambda\,(\nabla \cdot \mathbf{u}^{n,i,a-1})\,\mathbf{I}}{\left(1 - \left(\beta |\mathbb{E}^{1/2}\left[\boldsymbol{\epsilon}\right]|\right)^{\alpha}\right)^{1/\alpha}} \right) \colon \left(\frac{\nabla \boldsymbol{w} + \nabla \boldsymbol{w}^{\mathrm{T}}}{2}\right) \right). \end{aligned} \tag{54}$$

3.3.2. Step 2. Solve the phase-field subproblem

Secondly, the phase-field subproblem (Eq. (41)) is solved with the displacement and phase-field values given from the previous iteration $\{\mathbf{u}^{n,i}, \varphi^{n,i-1},$ and $\varphi^{n-1}\}$.

Given $\mathbf{u}^{n,i}$, $\varphi^{n,i-1}$, and φ^{n-1}, we seek for $\varphi_h^{n,i} \in W_h$ satisfying

$$A_2(\varphi_h^{n,i}, \psi) = 0, \quad \forall \psi \in W_h, \tag{55}$$

where

$$A_2(\varphi^{n,i},\psi) := (1-\kappa)(\varphi^{n,i}\boldsymbol{\sigma}(\mathbf{u}^{n,i}):\boldsymbol{\epsilon}(\mathbf{u}^{n,i}),\psi) - G_c(\frac{1}{\xi}(1-\varphi^{n,i}),\psi) + G_c(\xi\nabla\varphi^{n,i},\nabla\psi)$$
$$+(\eta^i(\omega_\gamma^{n,i}+\gamma(\varphi^{n,i}-\varphi^{n-1})),\psi) + L_\varphi(\varphi^{n,i}-\varphi^{n,i-1},\psi). \tag{56}$$

Here the last term is the L-scheme stabilization term with a positive constant value L_φ, and $\eta^i \in L^\infty(\Lambda)$ is defined as

$$\eta^i(x) := \begin{cases} 1, & \text{if } x = \omega_\gamma^{n,i} + \gamma(\varphi^{n,i}-\varphi^{n-1}) > 0, \\ 0, & \text{if } x = \omega_\gamma^{n,i} + \gamma(\varphi^{n,i}-\varphi^{n-1}) \le 0, \end{cases}$$

to replace the operator $[\cdot]^+$.

To solve the nonlinear problem of Eq. (55), we employ the Newton iteration algorithm coupled with an appropriate line search. Thus, we find $\delta\varphi^{n,i,b} \in W_h$ by solving

$$A_2'(\varphi^{n,i,b-1})(\delta\varphi^{n,i,b},\psi) = -A_2(\varphi^{n,i,b-1})(\psi), \quad \forall\psi \in V_h, \tag{57}$$

for the iterations step, $b = 1, 2, \ldots$, until $\|\delta\varphi^{n,i,b}\| \le \varepsilon_b$. Then we update

$$\varphi^{n,i,b} = \varphi^{n,i,b-1} + \omega_\varphi\,\delta\varphi^{n,i,b}, \tag{58}$$

in which ω_φ is a line search parameter and $\omega_\varphi \in [0,1]$. Here the Jacobian of A_2 applied to a direction of $\delta\varphi$ is

$$A_2'(\varphi^{n,i,b-1})(\delta\varphi^{n,i,b},\psi) := (1-\kappa)(\delta\varphi^{n,i,b}\;\boldsymbol{\sigma}(\mathbf{u}^{n,i}):\boldsymbol{\epsilon}(\mathbf{u}^{n,i}),\psi) + G_c(\frac{1}{\xi}\,\delta\varphi^{n,i,b},\psi)$$
$$+G_c(\xi\;\nabla\delta\varphi^{n,i,b},\nabla\psi) + \eta^i\gamma(\delta\varphi^{n,i,b},\psi) + L_\varphi(\delta\varphi^{n,i,b},\psi), \tag{59}$$

and

$$A_2(\varphi^{n,i,b-1})(\psi) := (1-\kappa)(\varphi^{n,i,b-1}\;\boldsymbol{\sigma}(\mathbf{u}^{n,i}):\boldsymbol{\epsilon}(\mathbf{u}^{n,i}),\psi) - G_c(\frac{1}{\xi}(1-\varphi^{n,i,b-1}),\psi)$$
$$+G_c(\xi\;\nabla\varphi^{n,i,b-1},\nabla\psi) + (\eta^i(\omega_\gamma^{n,i}+\gamma(\varphi^{n,i,b-1}-\varphi^{n-1})),\psi) + L_\varphi(\varphi^{n,i,b-1}-\varphi^{n,i-1},\psi). \tag{60}$$

If the Newton iteration converges, we set

$$\varphi^{n,i} = \varphi^{n,i,b}.$$

We note that the choice of the $\boldsymbol{\sigma}$ is either Eq. (48) for the linear case, or Eq. (49) for the nonlinear strain-limiting case, depending on the mechanics subproblem that we solve.

As we discussed in the previous section, the augmented-Lagrangian iteration is embedded in the L-scheme iteration. Thus, the augmented term $\omega_\gamma^{n,i}$ is updated every staggered step of i:

$$\omega_\gamma^{n,i} = [\omega_\gamma^{n,i-1} + \gamma(\varphi^{n,i,b-1}-\varphi^{n-1})]^+. \tag{61}$$

We also note that the phase-field function has three different categories for the iteration index: the previous time-step index $n-1$, the staggered step of the L-scheme iteration index i and $i-1$, and the Newton iteration index b and $b-1$. Meantime, the displacement value is given as $\mathbf{u}^{n,i}$, which is computed from the first step of the L-scheme, i.e., the mechanics subproblem.

Finally, we employ both the mechanics subproblem residual $\|A_1(\mathbf{u}^{n,i},\boldsymbol{w})\| \le \mathrm{T_{OL}}$ and the phase-field subproblem residual $\|A_2(\varphi_h^{n,i},\psi)\| \le \mathrm{T_{OL}}$, where $\mathrm{T_{OL}}$ is a tolerance value of the stopping criteria for both the L-scheme and the augmented Lagrangian. If the whole iteration converges, we obtain

$$\mathbf{u}^n = \mathbf{u}^{n,i,a} \quad \text{and} \quad \varphi^n = \varphi^{n,i,b}. \tag{62}$$

4. Numerical examples

In this final section, we present several numerical examples to verify the proposed nonlinear algorithm. Moreover, we illustrate the capabilities and the effectiveness of the framework compared to the linear elastic fracture mechanics (LEFM) model. The code extends IPACS [95], which is built on the open-source finite element package deal.II [96], to consider nonlinear elasticity. All the computations are performed utilizing high performance computing machines at Texas A&M University - Corpus Christi. For the nonlinear strain-limiting (NLSL) model, the computations are developed by the authors based on the previous studies [63,90].

From the displacement ($\mathbf{u}$) obtained from the governing equations coupled with the phase-field, i.e., Eq. (15) for the LEFM and Eq. (27) for the NLSL, the stress values are calculated using the Hooke's law (Eq. (17)) for both models. Each strain value calculation is based on each model: $\boldsymbol{\epsilon}$ from Eq. (13) for the LEFM, and $\boldsymbol{\epsilon}_{\mathrm{NL}}$ for the NLSL with Eq. (26). Note that if the nonlinear parameter β goes to zero in Eq. (26), then $\boldsymbol{\epsilon}_{\mathrm{NL}}$ is identical to $\boldsymbol{\epsilon}$ from Eq. (13) for the LEFM.

Table 1
Example 1. The results of L^2 error convergence test of the approximated displacement for the linear (LEFM) and the nonlinear (NLSL) mechanics subproblem are illustrated. We observe the optimal convergence for both cases.

Cycle	h	Linear		Nonlinear	
		L2 error	Rate	L2 error	Rate
1	0.25	0.033493958414	0.0	0.031402524561	0.0
2	0.125	0.008457780816	2.6942	0.007450392935	2.8163
3	0.0625	0.002119761659	2.3542	0.001790875453	2.4253
4	0.03125	0.000530273421	2.1788	0.000437507028	2.2160
5	0.015625	0.000132589164	2.0898	0.000108024578	2.1088
6	0.0078125	0.000033148594	2.0450	0.000026842623	2.0540

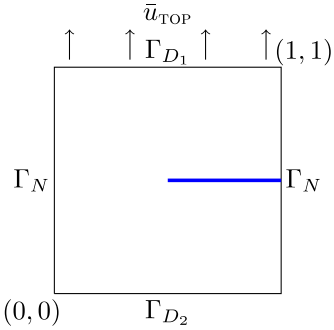

Fig. 3. Example 2. A setup and the boundary conditions: the blue line indicates the slit and the arrows on the top denote the axial traction.

4.1. Example 1: The error convergence tests

In the first example, the error convergence is tested to verify the implementation for the NLSL formulation presented in previous sections. For simplicity, only the mechanics subproblem is considered by neglecting the phase-field variable. Thus, we set the phase-field to be a constant one ($\varphi = 1$) and $\kappa = 0$ for the whole domain.

Here, the given exact solution for the mechanics subproblem is defined as

$$\mathbf{u}(x, y) := (\sin x \sin y, \cos x \cos y), \tag{63}$$

in the computational domain $\Lambda = [0, 1]^2$. The right hand side and the boundary conditions are chosen accordingly to satisfy the homogeneous boundary conditions on $\partial\Lambda$. In addition, Lamé coefficients are set as $\lambda = \mu = 0.01$ and the nonlinear parameters are given as $(\alpha, \beta) = (0.1, 0.1)$. Six computations on uniform meshes were computed where the mesh size h is divided by two for each cycle, and the corresponding number of cells for each cycle is 4, 16, 64, 256, 1024, and 4096.

The results of the $L^2(\Lambda)$ errors for the approximated displacement solution versus the mesh size h are shown in Table 1. We observe the expected optimal convergence rate for both linear and nonlinear cases for our mechanics subproblem.

4.2. Example 2: Strain-limiting effects for a static fracture

In this example, we compare the presented NLSL model with the LEFM model in a domain with a static fracture. In $\Lambda = [0, 1]^2$, the initial fracture is described as a slit on $(0.5, 0.5) - (1.0, 0.5)$. For the tensile crack in mode I, the Dirichlet boundary condition $\mathbf{u} = (0, \bar{u}_{\mathrm{TOP}})$ is employed on the top boundary, Γ_{D_1}, where the values of $\bar{u}_{\mathrm{TOP}}$ are chosen differently with respect to the test cases. On the bottom boundary, Γ_{D_2}, only the y-component is imposed with zero value but the x-component is traction-free. The homogeneous traction-free Neumann boundary condition is employed for the left and right boundaries, Γ_N, including the slit. See Fig. 3 for more details. The initial mesh is refined 7 times globally, thus $h = 0.0078125$. Moreover, we utilize the linear problem, i.e., the LEFM, for the initial guess for the first nonlinear Newton iteration of the NLSL to expedite the convergence.

Here, we test four different cases for the displacement values on the top boundary as $\bar{u}_{\mathrm{TOP}} = 2.0,\ 1.0,\ 0.5,$ and 0.1, corresponding to `CASE 1`, `CASE 2`, `CASE 3`, and `CASE 4`, respectively. As we discussed in Remark 2.4, a suitable nonlinear parameter pair of (α, β) should be chosen to satisfy the condition of Eq. (29). More precisely, we obtain

$$0 \le \beta < \left(\frac{1}{|\mathbb{E}^{1/2}[\boldsymbol{\epsilon}]|^{\alpha}} \right)^{1/\alpha}, \tag{64}$$

		$\bar{u}_{\text{TOP}}$	β	α
`CASE 1`	i	2.0	0.04	2
	ii			1
	iii			0.5
	iv			0.25
`CASE 2`	i	1.0	0.09	2
	ii			1
	iii			0.5
	iv			0.25
`CASE 3`	i	0.5	0.18	2
	ii			1
	iii			0.5
	iv			0.25
`CASE 4`	i	0.1	0.92	2
	ii			1
	iii			0.5
	iv			0.25

Fig. 4. Example 2. Different test cases for α and β.

and the condition simplifies to $\beta|\mathbb{E}^{1/2}[\boldsymbol{\epsilon}]| < 1$ by assuming $\alpha > 0$. In this case, we only need to satisfy $0 \leq \beta|\mathbb{E}^{1/2}[\boldsymbol{\epsilon}]| < 1$ for a given value of β. Therefore, by setting Lamé coefficients as $\lambda = \mu = 1.0$, the β values of maximum (rounding to 2 decimal places) for each cases are presented in Fig. 4 for each top boundary condition, $\bar{u}_{\text{TOP}}$, satisfying the condition in the inequality above with any given positive α.

Moreover, to investigate the effects of the modeling parameters (α, β) for the NLSL, we vary the choice for the α values. Starting with $\alpha = 2$, we arbitrarily set α reducing by half as shown in Fig. 4. Thus, we study a total of 16 different cases for the NLSL model, and 4 different cases for the LEFM (which are identical to the corresponding the NLSL models when $\beta = 0$) are also computed for the comparison. Eventually, we aim to see the maximized strain-limiting effect from the optimized combinations of (α, β).

To this end, we calculate the axial stress and strain along the center line, $(0, 0.5) - (0.5, 0.5)$, i.e., starting from the left boundary to the tip location of slit. The axial stress (σ_{22}) corresponds to the component of $\boldsymbol{\sigma}$ from the Hooke's law (Eq. (17) or $\mathbb{E}(\boldsymbol{\epsilon})$ in Eq. (28)), whereas the axial strain (ϵ_{22}) is calculated with the corresponding component of $\boldsymbol{\epsilon}$ or $\boldsymbol{\epsilon}_{\text{NL}}$. If we have $\beta = 0$ or $\alpha \to \infty$, then $\boldsymbol{\epsilon}_{\text{NL}}$ is identical to $\boldsymbol{\epsilon}$ for the LEFM, without any strain-limiting effect. Also note that we compute the average values of σ_{22} and ϵ_{22} in quadrature points for each cell.

First, Fig. 5 illustrates the axial stresses for each case by varying the α and β values as shown in Fig. 4. For each case, the stress values are compared with the LEFM, which is identical to the NLSL when $\beta = 0$. The overall pattern of stress growth near the crack-tip is a clear evidence that there is a near-tip stress concentration similar to the linear model. And the stress concentration is invariably observed even with different values of modeling parameters α and β.

On the other hand, Fig. 6 presents the strains along the same center line from the left boundary to the tip location of slit. Here, the axial strain values for each case are illustrated. We note that the obvious strain-limiting effect is shown by comparing with the values from the LEFM. The different effects are observed by different choice of α values. With this setup, the most strain-limiting effect occurs with the smallest value of $\alpha = 0.25$ given for each case. This is a consistent result from the theory that the NLSL becomes the LEFM if $\alpha \to \infty$.

Finally from this example, we observe that the stress–strain behavior in the neighborhood of the crack-tip, is sensitive to the choice of modeling parameters of (α, β) [29,76,77]. Thus, for calibration purpose with experiments for a certain material of specific mechanical parameters, one can choose the nonlinear parameters in the strain-limiting model by comparing the simulation results with the experimental data.

4.3. Example 3: A static phase-field fracture

In this example, we replace the fracture representation in Example 2 with the phase-field approach and investigate the NLSL model. Most of the setup is the same as the previous example, but here the phase-field variable (φ) is employed to describe the fracture. Thus, in the computational domain $\Lambda = [0, 1]^2$, a (prescribed) initial crack with length $l_0 = 0.5$ is placed on $(0.5, 1) \times (0.5 - h_{\min}, 0.5 + h_{\min}) \subset \Lambda$. The initial phase-field values are set to zero for the initial fracture described above and $\varphi = 1$ otherwise. This replaces the slit in the previous example.

The initial mesh is seven times uniformly refined as the previous example but here three additional levels of adaptive mesh refinement is employed near the fracture, where $\varphi < 0.9$, resulting in $h_{\min} = 0.0009765625$. For the phase-field, homogeneous Neumann condition is employed and the regularization parameters are chosen as $\xi = 2h_{\min}$, and $\kappa = 10^{-10}h_{\min}$. See Fig. 7 for more details.

The same displacement boundary conditions on Γ_{D_1} and Γ_{D_2} as the previous example are employed, but here we set $\bar{u}_{\text{TOP}} = 0.0001$. For the coupling between the mechanics and the phase-field, the presented L-scheme is utilized by

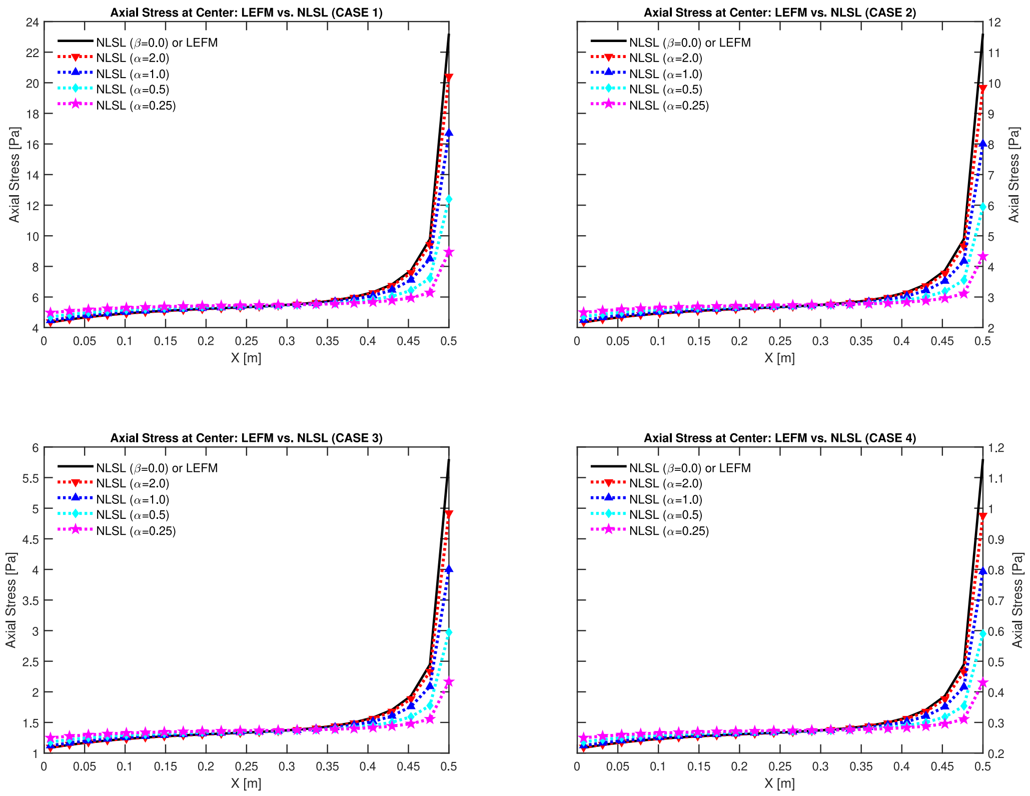

Fig. 5. Example 2. Axial stresses for each case from `CASE 1` (Top Left) to `CASE 4` (Bottom Right). Approaching to the crack-tip, X = 0.5, similar singular patterns for the stress values are shown in each case.

Table 2
Example 3. Different test cases for α and β.

		Fixed parameter	Value	Changing parameter	Value
CASE 1	i	β	127	α	2
	ii				1
	iii				0.5
CASE 2	i	α	0.25	β	1
	ii				10
	iii				50

choosing the L-constant as 10^{-6} for both the mechanics and the phase-field (i.e., $\mathrm{L}_u = \mathrm{L}_\phi = 10^{-6}$). The stopping criteria for the staggered L-scheme is $\mathrm{T}_{\mathrm{OL}} = 10^{-6}$, and the stopping criteria for the Newton's method for both the displacement and the phase-field are set as $\varepsilon_a = \varepsilon_b = 10^{-8}$. Note that for mechanics subproblem in the NLSL, only the first Newton iteration is utilizing the initial guess from the linear problem of the LEFM for faster convergence. In addition, the penalty parameter $\gamma = 10^4$ is set for the irreversibility condition. The critical energy release rate is chosen as $G_c = 5\,\mathrm{N\,m^{-1}}$. Then, all the other numerical and physical parameters are the same as the ones in the previous example.

With the given conditions above, here we investigate the effects of the nonlinear parameters for both (α, β). First, by Eq. (64), we obtained the maximum of β as $\beta_{\max} = 127$ for varying α. In addition, we varied the choice for the value of $\beta < \beta_{\max}$ by fixing the value of α. Thus, as shown in Table 2, we investigated the total 6 different cases for the NLSL model.

Fig. 8 presents the effect of our proposed nonlinear strain-limiting model with the phase-field approach. Here, the axial stress (σ_{22}) and strain (ϵ_{22}) values along the center line $(0, 0.5) - (0.5, 0.5)$ are computed for both the LEFM and the NLSL as the previous example, i.e., Example 2. Overall, the strain-limiting effect is well presented through each combination of (α, β) with the phase-field fracture. Especially, we observe the dramatic limiting effect of strain when $\alpha < 1.0$.

We note that the values of stress and strain are reduced near the crack-tip region (Fig. 8), due to the phase-field, since there is nearly no mechanics when $\varphi = 0$. In particular, the stress with the phase-field is defined as $\boldsymbol{\sigma}_\varphi := g(\varphi)\boldsymbol{\sigma} = ((1-\kappa)\varphi^2 + \kappa)\boldsymbol{\sigma}$, and the stress values approach to zero near the front of the phase-field crack-tip.

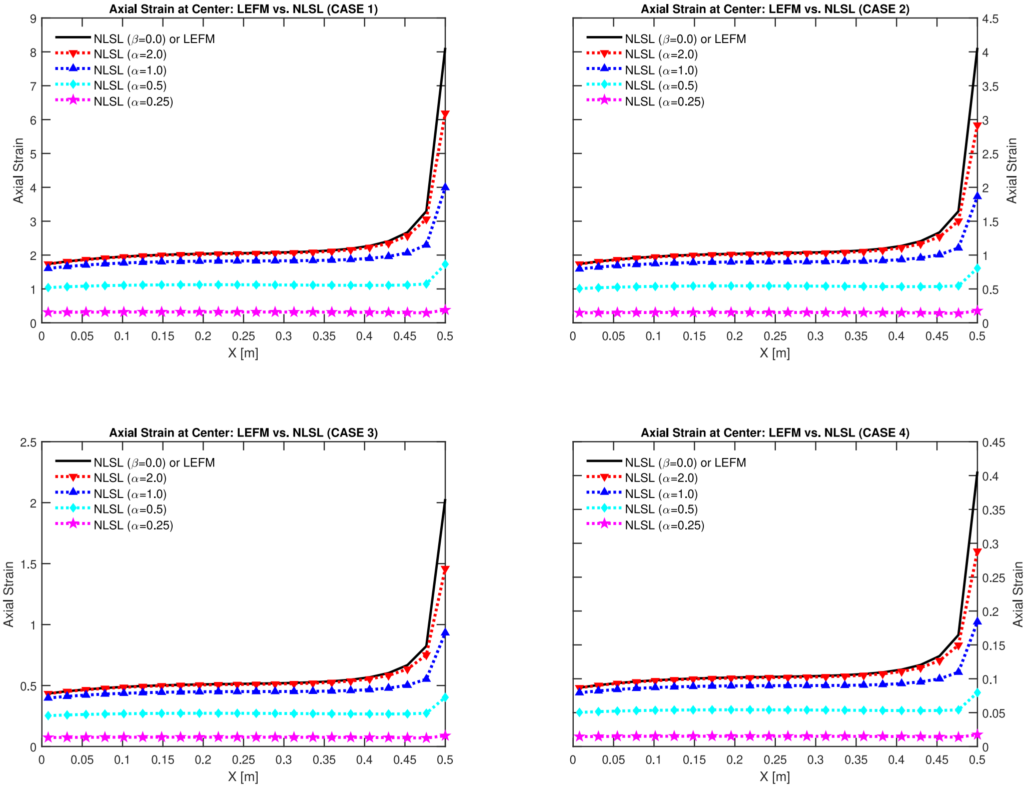

Fig. 6. Example 2. Axial strains for each case from `CASE 1` (Top Left) to `CASE 4` (Bottom Right). With smaller values of α, strain is distinctively limited for the nonlinear strain-limiting (NLSL) model in each case.

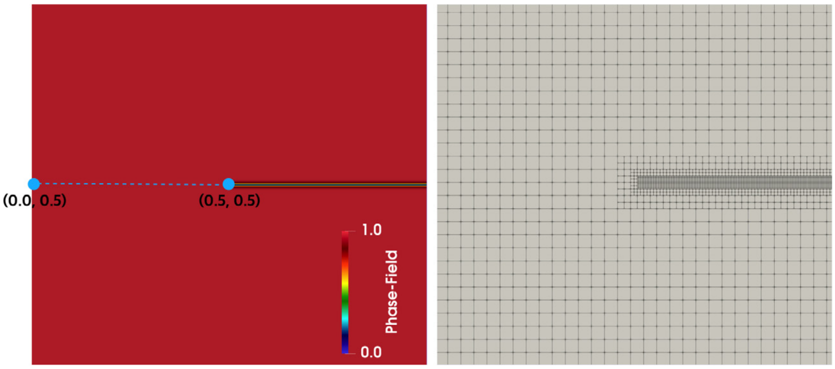

Fig. 7. Example 3. (Left) illustrates the setup with an initial phase-field fracture. As the previous example, the stress and strain values are plotted on the dashed line (0.0, 0.5)-(0.5,0.5). (Right) adaptive mesh refinement is employed near the fracture.

4.4. Example 4: A quasi-static propagating fracture

In this final example, we consider the fracture propagation by employing the quasi-static phase-field approach with the given boundary condition for each timestep. The basic setup including the initial and boundary conditions is similar to Example 2 (See Fig. 3), but in this example, we march the timesteps to propagate the given fracture. The timestep size is chosen as $\Delta t = 0.0001$ and we set $\bar{u}_{\text{TOP}} = t$, thus the displacement imposed at the top boundary is increased by marching the timesteps. The total number of timesteps is set to $N = 50$, which is enough to observe the full propagation of the fracture toward the left end. The initial mesh is refined 7 times globally and we pre-refine around the expected crack path ($0.0 \leq x \leq 0.6$, $0.4 < y < 0.6$) locally for two more levels. Here, $h_{\min} = 0.002$ and we set Lamé coefficients as $\lambda = 121.15$ kPa, $\mu = 80.77$ kPa with $G_c = 1\,\text{N}\,\text{m}^{-1}$.

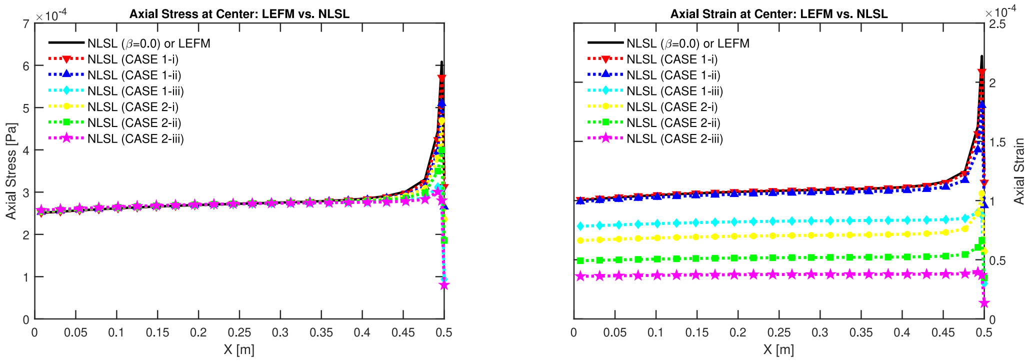

Fig. 8. Example 3. Axial stress (Left) and strain (Right) values for each case. We observe the strain-limiting effect near the tip of phase-field fracture with an appropriate choice of α and β.

Table 3
Example 4. Newton iteration numbers for each subproblem in the LEFM and the NLSL at the time $t = 0.001$ ($n = 20$ is not here)

Model	Subproblem	$t = 0.001$	$t = 0.002$	$t = 0.003$
LEFM	Mechanics	3	3	5
	Phase-field	2	2	4
NLSL	Mechanics	7	13	182
	Phase-field	4	4	60

For the NLSL model, we set the nonlinear parameter pair as $(\alpha, \beta) = (0.25, 4.8 \times 10^{-4})$ to satisfy the condition Eq. (64). Since the displacement load is increased in every timestep, we take the minimum of β for the entire timesteps. Then, we note that the condition from Eq. (64) is enforced throughout the whole simulation. The same Newton iteration tolerance and staggered L-scheme coefficients as the previous example (Example 3) are chosen, and the penalty parameter for the irreversibility condition is set as $\gamma = 10^{-7}$.

First, Figs. 9 and 10 illustrate the propagation of the fracture with the phase-field values for the LEFM and the NLSL, respectively. We observe that the NLSL model initiates the fracture earlier than the LEFM. In addition, the overall distribution patterns of axial strain (ε_{22}) values are different. For the LEFM, it is only concentrated near the vicinity of the crack-tip with quite larger (around 3 to 5 times) values than the NLSL. Meanwhile, the NLSL has more distributed values over the domain, relatively avoiding the singular strain in front of the tip.

Fig. 11 illustrates the comparisons of the axial stress (Left) and axial strain (Right) values at the center line of $(0, 0.5) - (0.5, 0.5)$ between the LEFM and the NLSL models for 3 different times (snapshots) of simulations. From (Top) row through (Middle) to (Bottom) row, the timesteps of $n = 10$, 20, and 30, respectively, are presented for axial stress (σ_{22}) and strain (ε_{22}) values. We emphasize that the expected strain-limiting effects are observed from the NLSL model and these results also illustrate that the proposed strain-limiting model initiates the fracture propagation earlier than the LEFM model. For the NLSL model, the crack-tip has moved forward around $n = 30$ and the stress and strain values near the tip are decreased due to the crack initiation with the phase-field function.

Regarding the same timesteps, we present in Table 3 the total Newton iteration numbers for each subproblem (A_1 of the mechanics subproblem and A_2 of the phase-field subproblem in Eqs. (40) and (41), respectively) within each method. The Newton iteration counts here are during the whole span of the L-scheme including the augmented Lagrangian for each subproblem until the whole problem converges within each timestep. Thus, it counts till obtaining the solutions ($\mathbf{u}^n$ and φ^n) as Eq. (62) by satisfying $\mathrm{T_{OL}}$ in the corresponding timestep. Note that the NLSL has several times more iterations overall due to the nonlinearity and also that the nonlinearity gets severer when the phase-field crack starts to grow and propagate at $t = 0.003$ ($n = 30$). Even for the LEFM, the phase-field crack growth (although not presented here) requires much more iterations (more than 10 times) than the static state shown with $t = 0.001$ ($n = 10$), $t = 0.002$ ($n = 20$), and $t = 0.003$ ($n = 30$).

In this example, we are also interested in the bulk (or strain) energy, the crack (or surface) energy, and the total energy. The total energy is defined as

$$E_{\epsilon} := \text{Total Energy} = \text{Bulk Energy} + \text{Surface Energy}, \tag{65}$$

and we have two different bulk energy formulations. For the LEFM, we have

$$\text{Linear Bulk Energy} := \int_{\Lambda} \frac{((1-\kappa)\varphi^2 + \kappa)}{2} \left[2\mu \boldsymbol{\epsilon}(\mathbf{u}) \colon \boldsymbol{\epsilon}(\mathbf{u}) + \lambda\, (\nabla \cdot \mathbf{u})^2 \right] \, d\mathbf{x}, \tag{66}$$

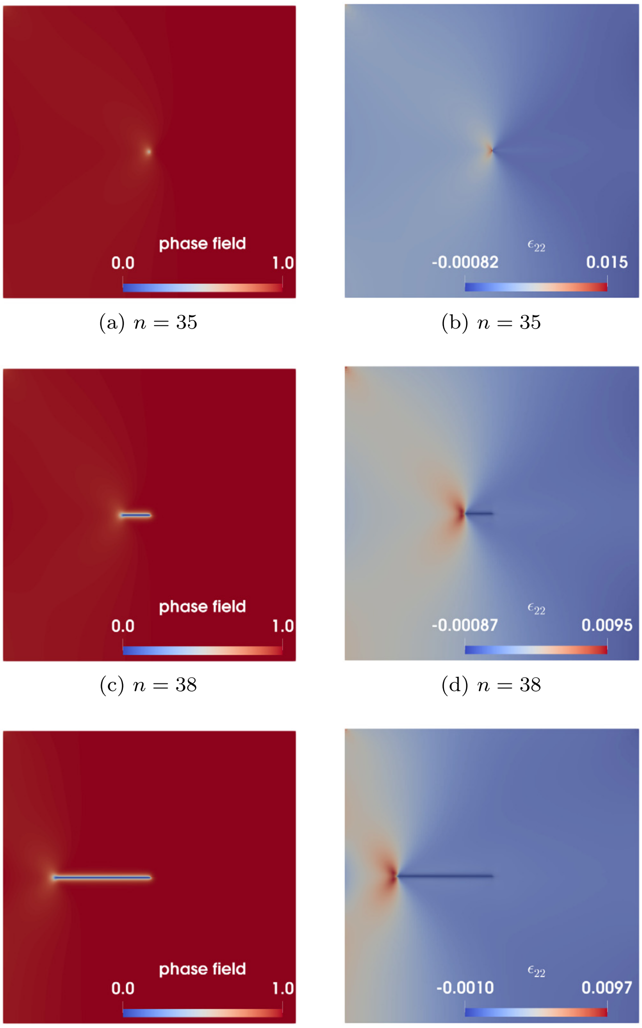

(a) $n = 35$ (b) $n = 35$

(c) $n = 38$ (d) $n = 38$

(e) $n = 42$ (f) $n = 42$

Fig. 9. Example 4. (Left) illustrates the phase-field values during crack evolution for each timestep with the LEFM. (Right) present the corresponding ϵ_{22} values for each case. The dark blue line indicates the corresponding fracture (phase-field) from (Left).

and for the NLSL (based on Eq. (27)) we have,

$$\text{Nonlinear Bulk Energy} := \int_{\Lambda} \frac{((1-\kappa)\varphi^2+\kappa)}{2} \frac{\left[2\mu\boldsymbol{\epsilon}(\mathbf{u}) : \boldsymbol{\epsilon}(\mathbf{u}) + \lambda\,(\nabla\cdot\mathbf{u})^2\right]}{(1-\beta^{\alpha}|\mathbb{E}^{1/2}(\mathbf{u})|^{\alpha})^{1/\alpha}}\, d\mathbf{x}, \tag{67}$$

where κ is a regularization parameter taken as $\kappa = 10^{-10}h_{\text{min}}$. For this example, we have the Lamé coefficients as $\lambda = 121.15$ kPa, $\mu = 80.77$ kPa. On the other hand, the crack energy is defined as

$$\text{Crack Energy} := \frac{G_c}{2}\int_{\Lambda}\left[\frac{(1-\varphi)^2}{\xi} + \xi|\nabla\varphi|^2\right] d\mathbf{x}, \tag{68}$$

where $\xi = 2h_{\text{min}}$, and the critical energy release rate (Griffith's criteria) is $G_c = 1\,\text{N}\,\text{m}^{-1}$.

Fig. 12 (Left) presents the comparisons of bulk and crack energies following the above definitions between the LEFM and the NLSL models. Fig. 12 (Right) represents the evolution of crack-tip speed as a function of time, which is computed approximately by the discrete variation of the crack–surface energy given in Eq. (68). We see the crack-tip speed depends linearly on the loading speed ($\bar{u}_{\text{TOP}} = t$), since the quasi-static problem is considered in this work. It is also clear that the crack-tip sprints immediately after the initiation from the original slit. The same is hinted in the decrease of bulk energy as depicted in Fig. 12 (Left) in both models. As seen in Fig. 12 (Left) and (Right), we highlight a possibility of deviation

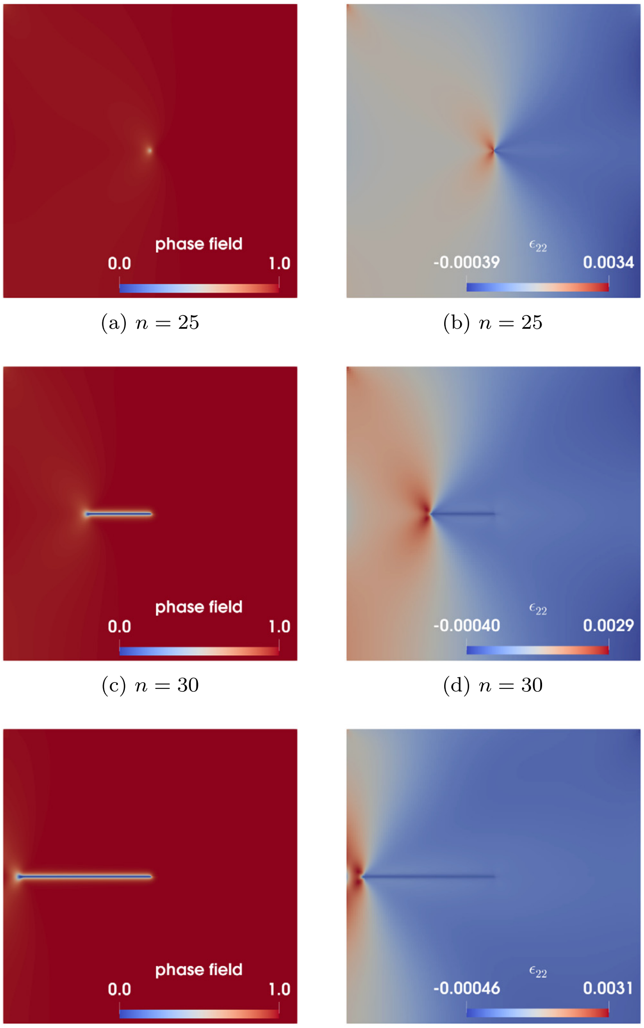

(a) $n = 25$ (b) $n = 25$

(c) $n = 30$ (d) $n = 30$

(e) $n = 33$ (f) $n = 33$

Fig. 10. Example 4. (Left) illustrates the phase-field values during crack evolution for each timestep with the NLSL model. (Right) presents the corresponding ϵ_{22} values for each case. The blue (lighter and thinner than the LEFM) line indicates the corresponding fracture (phase-field) from (Left). We note that the ϵ_{22} values are smaller than the LEFM.

for the NLSL model compared to the LEFM model in the crack propagation speed along with the bulk/crack energies. However, any validation of the different crack-tip speed between the LEFM and the NLSL is a future work.

5. Conclusion

In this paper, we investigate the strain-limiting nonlinear elasticity model coupled with the phase-field for the quasi-static tensile fracture propagation. A Newton iteration is employed for the nonlinear mechanics and the phase-field equations, and an iterative L-scheme is utilized for coupling of the corresponding subproblems. The augmented Lagrangian method is employed for the constrained minimization problem which accommodates the irreversibility condition of the phase-field variable. Several numerical results for propagating fractures, under the mode I loading, illustrate the performance of our algorithm with the capabilities of the computational framework. It is shown that using the proposed strain-limiting framework to model any bulk material of strain-limiting guarantees to bound the crack-tip strains even with the singular stresses. Although the presented strain-limiting model requires a careful selection for the modeling parameters α and β, any reasonable choice can illustrate the desired limited strain. Future work can include a pertinent validation of the current strain-limiting model for the real experimental data, extending the model to consider more freedom for the choice of the parameters, along with enhancing the capability of nonlinear solver.

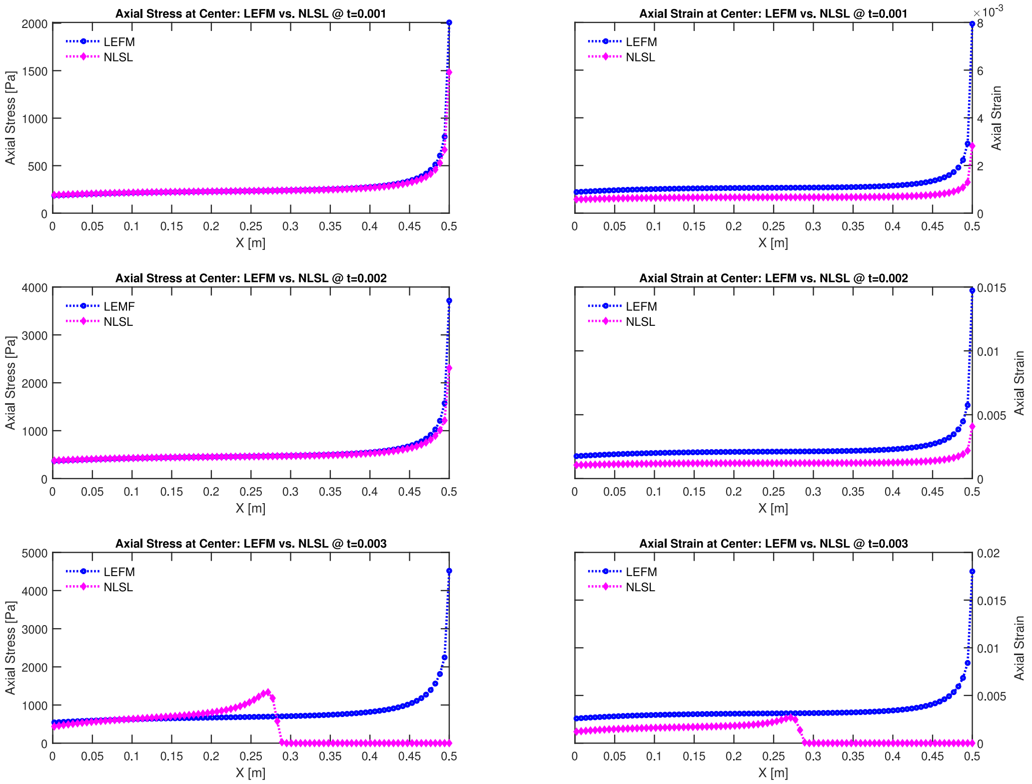

Fig. 11. Example 4. Comparisons of axial stress σ_{22} (Left) and strain ϵ_{22} (Right) values between the LEFM and the NLSL models at the time $t = 0.001$ (Top), 0.002 (Middle), and 0.003 (Bottom). We observe the strain-limiting effect near the tip of the fracture for the NLSL model when the fracture propagation is initiated before $t = 0.003$ for the NLSL.

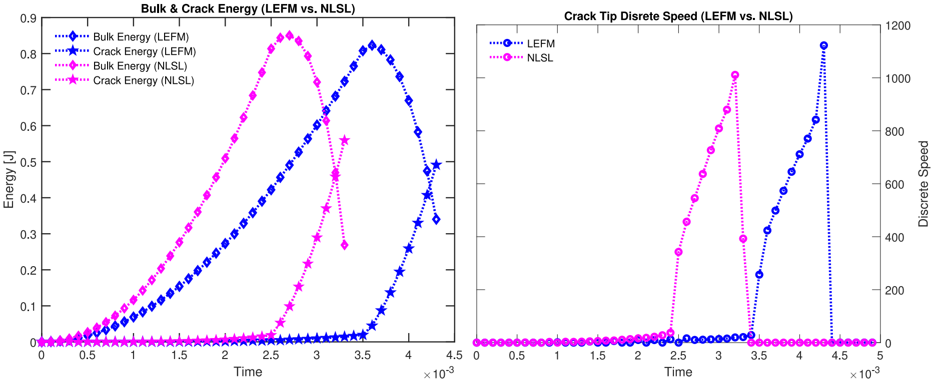

Fig. 12. Example 4. (Left) Comparisons of the bulk and crack energy between the LEFM and the NLSL models. (Right) The discrete crack-tip speed computed as a derivative of the crack surface energy as a function of time.

Acknowledgments

This research done by S. Lee is based upon work supported by the National Science Foundation, USA under Grant No. NSF DMS-1913016. Other authors, Hyun C. Yoon and S. M. Mallikarjunaiah, would like to thank the support of College of Science & Engineering, Texas A&M University-Corpus Christi. Lastly, Hyun C. Yoon, was supported in part by the basic research fund (Project No. GP2020-006) of Korea Institute of Geoscience and Mineral Resources (KIGAM).

References

[1] A.A. Griffith, The phenomena of rupture and flow in solids, Phil. Trans. R. Soc. A 221 (1921) 163–198.
[2] K.B. Broberg, Cracks and Fracture, Academic Press, 1999.

[3] J. Knowles, E. Sternberg, Large deformations near a tip of an interface-crack between two neo-hookean sheets, J. Elasticity 13 (3) (1983) 257–293.
[4] G.I. Barenblatt, The mathematical theory of equilibrium cracks in brittle fracture, Adv. Appl. Mech. 7 (1962) 55–129.
[5] M.E. Gurtin, A.I. Murdoch, A continuum theory of elastic material surfaces, Arch. Ration. Mech. Anal. 57 (4) (1975) 291–323.
[6] C. Kim, P. Schiavone, C.-Q. Ru, The effects of surface elasticity on an elastic solid with mode-III crack: complete solution, J. Appl. Mech. 77 (2) (2010) 021011.
[7] Y. Antipov, P. Schiavone, Integro-differential equation for a finite crack in a strip with surface effects, Q. J. Mech. Appl. Math. 64 (1) (2011) 87–106.
[8] A.Y. Zemlyanova, The effect of a curvature-dependent surface tension on the singularities at the tips of a straight interface crack, Quart. J. Mech. Appl. Math. 66 (2) (2013) 199–219.
[9] A.Y. Zemlyanova, J.R. Walton, Modeling of a curvilinear planar crack with a curvature-dependent surface tension, SIAM J. Appl. Math. 72 (5) (2012) 1474–1492.
[10] J.R. Walton, Plane-strain fracture with curvature-dependent surface tension: mixed-mode loading, J. Elasticity 114 (1) (2014) 127–142.
[11] T. Sendova, J.R. Walton, A new approach to the modeling and analysis of fracture through extension of continuum mechanics to the nanoscale, Math. Mech. Solids 15 (3) (2010) 368–413.
[12] L.A. Ferguson, M. Muddamallappa, J.R. Walton, Numerical simulation of mode-III fracture incorporating interfacial mechanics, Int. J. Fract. 192 (1) (2015) 47–56.
[13] J.R. Walton, M. Muddamallappa, Plane strain fracture with surface mechanics: non-local boundary regularization, in: International Congress of Theoretical and Applied Mechanics, Vol. XXIV, 2016.
[14] S. Zhang, S. Li, M. Jia, Y. Hao, R. Yang, Fatigue properties of a multifunctional titanium alloy exhibiting nonlinear elastic deformation behavior, Scr. Mater. 60 (8) (2009) 733–736.
[15] T. Saito, T. Furuta, J.-H. Hwang, S. Kuramoto, K. Nishino, N. Suzuki, R. Chen, A. Yamada, K. Ito, Y. Seno, T. Nonaka, H. Ikehata, N. Nagasako, C. Iwamoto, Y. Ikuhara, T. Sakuma, Multifunctional alloys obtained via a dislocation-free plastic deformation mechanism, Science 300 (5618) (2003) 464–467.
[16] F. Hou, S. Li, Y. Hao, R. Yang, Nonlinear elastic deformation behaviour of Ti–30Nb–12Zr alloys, Scr. Mater. 63 (1) (2010) 54–57.
[17] E. Withey, M. Jin, A. Minor, S. Kuramoto, D. Chrzan, J. Morris, The deformation of ‘Gum Metal’ in nanoindentation, Mater. Sci. Eng. A 493 (1) (2008) 26–32.
[18] V. Devendiran, R. Sandeep, K. Kannan, K. Rajagopal, A thermodynamically consistent constitutive equation for describing the response exhibited by several alloys and the study of a meaningful physical problem, Int. J. Solids Struct. 108 (2017) 1–10.
[19] V. Kulvait, J. Málek, K. Rajagopal, Modeling gum metal and other newly developed titanium alloys within a new class of constitutive relations for elastic bodies., Arch. Mech. 69 (3) (2017).
[20] K.R. Rajagopal, On implicit constitutive theories, Appl. Math. 48 (4) (2003) 279–319.
[21] K. Rajagopal, The elasticity of elasticity, Z. Angew. Math. Phys. 58 (2) (2007) 309–317.
[22] K. Rajagopal, A. Srinivasa, On the response of non-dissipative solids, in: Proceedings of the Royal Society of London A: Mathematical, Physical and Engineering Sciences, Vol. 463, (2078) The Royal Society, 2007, pp. 357–367.
[23] K. Rajagopal, Non-linear elastic bodies exhibiting limiting small strain, Math. Mech. Solids 16 (1) (2011) 122–139.
[24] K. Rajagopal, Conspectus of concepts of elasticity, Math. Mech. Solids 16 (5) (2011) 536–562.
[25] K. Rajagopal, On the nonlinear elastic response of bodies in the small strain range, Acta Mech. 225 (6) (2014) 1545–1553.
[26] M. Bulíček, J. Málek, K. Rajagopal, E. Süli, On elastic solids with limiting small strain: modelling and analysis, EMS Surv. Math. Sci. 1 (2) (2014) 293–342.
[27] M. Bulíček, J. Málek, K.R. Rajagopal, J.R. Walton, Existence of solutions for the anti-plane stress for a new class of ‘‘strain-limiting’’ elastic bodies, Calc. Var. Partial Differential Equations 54 (2) (2015) 2115–2147.
[28] M. Bulíček, J. Málek, E. Süli, Analysis and approximation of a strain-limiting nonlinear elastic model, Math. Mech. Solids 20 (1) (2015) 92–118.
[29] A. Bonito, V. Girault, E. Suli, Finite element approximation of a strain-limiting elastic model, 2018, arXiv preprint arXiv:1805.04006.
[30] N. Gelmetti, E. Suli, Spectral approximation of a strain-limiting nonlinear elastic model, Mat. Vesnik 71 (1–2) (2018).
[31] R. Bustamante, Some topics on a new class of elastic bodies, Proc. R. Soc. Lond. Ser. A Math. Phys. Eng. Sci. 465 (2105) (2009) 1377–1392.
[32] R. Bustamante, K. Rajagopal, A note on plane strain and plane stress problems for a new class of elastic bodies, Math. Mech. Solids 15 (2) (2010) 229–238.
[33] R. Bustamante, K. Rajagopal, Solutions of some simple boundary value problems within the context of a new class of elastic materials, Int. J. Non-Linear Mech. 46 (2) (2011) 376–386.
[34] R. Bustamante, K. Rajagopal, On a new class of electroelastic bodies. I, Proc. R. Soc. Lond. Ser. A Math. Phys. Eng. Sci. 469 (2149) (2013) 20120521.
[35] R. Bustamante, K. Rajagopal, Implicit constitutive relations for nonlinear magnetoelastic bodies, Proc. R. Soc. Lond. Ser. A Math. Phys. Eng. Sci. 471 (2175) (2015) 20140959.
[36] R. Bustamante, K. Rajagopal, Implicit equations for thermoelastic bodies, Int. J. Non-Linear Mech. 92 (2017) 144–152.
[37] A. Griffith, The phenomena of rupture and flow in solids., Philos. Trans. R. Soc. Lond. 221 (1921) 163–198.
[38] G. Barenblatt, The Mathematical Theory of Equilibrium Cracks in Brittle Fracture, in: Advances in Applied Mechanics, Vol. 7, Elsevier, 1962, pp. 55–129.
[39] B. Bourdin, J.-J. Marigo, C. Maurini, P. Sicsic, Morphogenesis and propagation of complex cracks induced by thermal shocks, Phys. Rev. Lett. 112 (2014) 014301.
[40] C. Miehe, L.-M. Schaenzel, H. Ulmer, Phase field modeling of fracture in multi-physics problems. Part I. Balance of crack surface and failure criteria for brittle crack propagation in thermo-elastic solids, Comput. Methods Appl. Mech. Engrg. 294 (2015) 449–485.
[41] N. Noii, T. Wick, A phase-field description for pressurized and non-isothermal propagating fractures, Comput. Methods Appl. Mech. Engrg. 351 (2019) 860–890.
[42] S. Lee, J.E. Reber, N.W. Hayman, M.F. Wheeler, Investigation of wing crack formation with a combined phase-field and experimental approach, Geophys. Res. Lett. 43 (15) (2016) 7946–7952.
[43] A. Mikelić, M.F. Wheeler, T. Wick, A quasi-static phase-field approach to pressurized fractures, Nonlinearity 28 (5) (2015) 1371–1399.
[44] T. Wick, S. Lee, M.F. Wheeler, 3D phase-field for pressurized fracture propagation in heterogeneous media, in: VI International Conference on Computational Methods for Coupled Problems in Science and Engineering 2015 Proceedings, 2015.
[45] A. Mikelić, M.F. Wheeler, T. Wick, A phase-field method for propagating fluid-filled fractures coupled to a surrounding porous medium, SIAM Multiscale Model. Simul. 13 (1) (2015) 367–398.
[46] S. Lee, M.F. Wheeler, T. Wick, Pressure and fluid-driven fracture propagation in porous media using an adaptive finite element phase field model, Comput. Methods Appl. Mech. Engrg. 305 (2016) 111–132.
[47] C. Miehe, S. Mauthe, Phase field modeling of fracture in multi-physics problems. Part III. crack driving forces in hydro-poro-elasticity and hydraulic fracturing of fluid-saturated porous media, Comput. Methods Appl. Mech. Engrg. 304 (2016) 619–655.

[48] Y. Heider, B. Markert, A phase-field modeling approach of hydraulic fracture in saturated porous media, Mech. Res. Commun. 80 (2017) 38–46, Multi-Physics of Solids at Fracture.

[49] S. Lee, A. Mikelić, M. Wheeler, T. Wick, Phase-field modeling of two phase fluid filled fractures in a poroelastic medium, Multiscale Model. Simul. 16 (4) (2018) 1542–1580.

[50] S. Lee, M.F. Wheeler, T. Wick, Iterative coupling of flow, geomechanics and adaptive phase-field fracture including level-set crack width approaches, J. Comput. Appl. Math. 314 (2017) 40–60.

[51] S. Lee, A. Mikelić, M.F. Wheeler, T. Wick, Phase-field modeling of proppant-filled fractures in a poroelastic medium, Comput. Methods Appl. Mech. Engrg. 312 (2016) 509–541, Phase Field Approaches to Fracture.

[52] T. Cajuhi, L. Sanavia, L. De Lorenzis, Phase-field modeling of fracture in variably saturated porous media, Comput. Mech. (2017).

[53] S. Lee, M.F. Wheeler, T. Wick, S. Srinivasan, Initialization of phase-field fracture propagation in porous media using probability maps of fracture networks, Mech. Res. Commun. 80 (2017) 16–23, Multi-Physics of Solids at Fracture.

[54] M.F. Wheeler, S. Srinivasan, S. Lee, M. Singh, et al., Unconventional reservoir management modeling coupling diffusive zone/phase field fracture modeling and fracture probability maps, in: SPE Reservoir Simulation Conference, Society of Petroleum Engineers, 2019.

[55] J. Choo, W. Sun, Cracking and damage from crystallization in pores: Coupled chemo-hydro-mechanics and phase-field modeling, Comput. Methods Appl. Mech. Engrg. 335 (2018) 347–379.

[56] C. Chukwudozie, B. Bourdin, K. Yoshioka, A variational phase-field model for hydraulic fracturing in porous media, Comput. Methods Appl. Mech. Engrg. 347 (2019) 957–982.

[57] K. Yoshioka, F. Parisio, D. Naumov, R. Lu, O. Kolditz, T. Nagel, Comparative verification of discrete and smeared numerical approaches for the simulation of hydraulic fracturing, GEM - Int. J. Geomath. 10 (1) (2019) 13.

[58] M. Ambati, T. Gerasimov, L. De Lorenzis, Phase-field modeling of ductile fracture, Comput. Mech. 55 (5) (2015) 1017–1040.

[59] I. Shovkun, D.N. Espinoza, Propagation of toughness-dominated fluid-driven fractures in reactive porous media, Int. J. Rock Mech. Min. Sci. 118 (2019) 42–51.

[60] S. Lee, B. Min, M.F. Wheeler, Optimal design of hydraulic fracturing in porous media using the phase field fracture model coupled with genetic algorithm, Comput. Geosci. 22 (3) (2018) 833–849.

[61] T.K. Mandal, V.P. Nguyen, A. Heidarpour, Phase field and gradient enhanced damage models for quasi-brittle failure: A numerical comparative study, Eng. Fract. Mech. 207 (2019) 48–67.

[62] S. Shiozawa, S. Lee, M.F. Wheeler, The effect of stress boundary conditions on fluid-driven fracture propagation in porous media using a phase-field modeling approach, Int. J. Numer. Anal. Methods Geomech. 43 (6) (2019) 1316–1340.

[63] M.K. Brun, T. Wick, I. Berre, J.M. Nordbotten, F.A. Radu, An iterative staggered scheme for phase field brittle fracture propagation with stabilizing parameters, Comput. Methods Appl. Mech. Engrg. 361 (2020) 112752.

[64] T. Heister, M.F. Wheeler, T. Wick, A primal-dual active set method and predictor-corrector mesh adaptivity for computing fracture propagation using a phase-field approach, Comput. Methods Appl. Mech. Engrg. 290 (2015) 466–495.

[65] K. Rajagopal, A. Srinivasa, On a class of non-dissipative materials that are not hyperelastic, in: Proceedings of the Royal Society of London A: Mathematical, Physical and Engineering Sciences, Vol. 465, (2102) The Royal Society, 2009, pp. 493–500.

[66] C. Truesdell, W. Noll, The non-linear field theories of mechanics, in: The Non-Linear Field Theories of Mechanics, Springer, Berlin, Heidelberg, 2004, pp. 1–579.

[67] C. Truesdell, Hypo-elasticity, J. Ration. Mech. Anal. 4 (1955) 83–1020.

[68] M. Carroll, Must elastic materials be hyperelastic?, Math. Mech. Solids 14 (4) (2009) 369–376.

[69] A. Spencer, Part III. Theory of invariants, Contin. Phys. 1 (2017) 239–353.

[70] K. Rajagopal, J. Walton, Modeling fracture in the context of a strain-limiting theory of elasticity: A single anti-plane shear crack, Int. J. Fract. 169 (1) (2011) 39–48.

[71] K. Gou, M. Mallikarjuna, K. Rajagopal, J. Walton, Modeling fracture in the context of a strain-limiting theory of elasticity: A single plane-strain crack, Internat. J. Engrg. Sci. 88 (2015) 73–82.

[72] S.M. Mallikarjunaiah, J.R. Walton, On the direct numerical simulation of plane-strain fracture in a class of strain-limiting anisotropic elastic bodies, Int. J. Fract. 192 (2) (2015) 217–232.

[73] T. Mai, J.R. Walton, On monotonicity for strain-limiting theories of elasticity, J. Elasticity 120 (1) (2015) 39–65.

[74] T. Mai, J.R. Walton, On strong ellipticity for implicit and strain-limiting theories of elasticity, Math. Mech. Solids 20 (2) (2015) 121–139.

[75] T. Mai, J.R. Walton, On strong ellipticity for implicit and strain-limiting theories of elasticity, Math. Mech. Solids 20 (2) (2015) 121–139.

[76] S. Fu, E. Chung, T. Mai, Generalized multiscale finite element method for a strain-limiting nonlinear elasticity model, J. Comput. Appl. Math. 359 (2019) 153–165.

[77] S. Fu, E. Chung, T. Mai, Constraint energy minimizing generalized multiscale finite element method for nonlinear poroelasticity and elasticity, 2019, arXiv preprint arXiv:1909.13267.

[78] M.S. Muddamallappa, On Two Theories for Brittle Fracture: Modeling and Direct Numerical Simulations (Ph.D. thesis), Texas A&M University, 2015.

[79] H.C. Yoon, S. Lee, S. Mallikarjunaiah, Quasi-static anti-plane shear crack propagation in nonlinear strain-limiting elastic solids using phase-field approach, Int. J. Fract. 227 (2021) 153–172.

[80] A. Ortiz, R. Bustamante, K. Rajagopal, A numerical study of a plate with a hole for a new class of elastic bodies, Acta Mech. 223 (9) (2012) 1971–1981.

[81] V. Kulvait, J. Málek, K. Rajagopal, Anti-plane stress state of a plate with a V-notch for a new class of elastic solids, Int. J. Fract. 179 (1–2) (2013) 59–73.

[82] V. Kulvait, J. Málek, K. Rajagopal, The state of stress and strain adjacent to notches in a new class of nonlinear elastic bodies, J. Elasticity 135 (1–2) (2019) 375–397.

[83] B. Bourdin, G. Francfort, J.-J. Marigo, Numerical experiments in revisited brittle fracture, J. Mech. Phys. Solids 48 (4) (2000) 797–826.

[84] G. Francfort, J.-J. Marigo, Revisiting brittle fracture as an energy minimization problem, J. Mech. Phys. Solids 46 (8) (1998) 1319–1342.

[85] L. Ambrosio, V. Tortorelli, Approximation of functionals depending on jumps by elliptic functionals via Γ-convergence, Comm. Pure Appl. Math. 43 (1990) 999–1036.

[86] L. Ambrosio, V. Tortorelli, On the approximation of free discontinuity problems, Boll. Unione Mat. Ital. B 6 (1992) 105–123.

[87] C. Miehe, F. Welschinger, M. Hofacker, Thermodynamically consistent phase-field models of fracture: variational principles and multi-field FE implementations, Int. J. Numer. Methods Eng. 83 (2010) 1273–1311.

[88] G.A. Francfort, C.J. Larsen, Existence and convergence for quasi-static evolution in brittle fracture, Comm. Pure Appl. Math. 56 (10) (2003) 1465–1500.

[89] A. Giacomini, Ambrosio-Tortorelli approximation of quasi-static evolution of brittle fractures, Calc. Var. Partial Differential Equations 22 (2) (2005) 129–172.

[90] M.F. Wheeler, T. Wick, W. Wollner, An augmented-Lagrangian method for the phase-field approach for pressurized fractures, Comput. Methods Appl. Mech. Engrg. 271 (2014) 69–85.

[91] M. Fortin, R. Glowinski, Augmented Lagrangian Methods: Applications to the Numerical Solution of Boundary-Value Problems, Vol. 15, Elsevier, 2000.

[92] R. Glowinski, P. Le Tallec, Augmented Lagrangian and Operator-Splitting Methods in Nonlinear Mechanics, Vol. 9, SIAM, 1989.

[93] I. Neitzel, T. Wick, W. Wollner, An optimal control problem governed by a regularized phase-field fracture propagation model, SIAM J. Control Optim. 55 (4) (2017) 2271–2288.

[94] A. Mikelić, M. Wheeler, T. Wick, Phase-field modeling through iterative splitting of hydraulic fractures in a poroelastic medium, GEM-Int. J. Geomath. 10 (1) (2019) 2.

[95] M.F. Wheeler, T. Wick, S. Lee, IPACS: Integrated phase-field advanced crack propagation simulator. An adaptive, parallel, physics-based-discretization phase-field framework for fracture propagation in porous media, Comput. Methods Appl. Mech. Engrg. 367 (2020) 113124.

[96] D. Arndt, W. Bangerth, T.C. Clevenger, D. Davydov, M. Fehling, D. Garcia-Sanchez, G. Harper, T. Heister, L. Heltai, M. Kronbichler, R.M. Kynch, M. Maier, J.-P. Pelteret, B. Turcksin, D. Wells, The deal.II library, version 9.1, J. Numer. Math. (2019) accepted.